

**OSSE Preprint No. 6**

**The Oriented Scintillation  
Spectrometer Experiment  
Instrument Description**

To appear in *Astrophysical Journal Supplements*

Report Documentation Page				Form Approved OMB No. 0704-0188	
Public reporting burden for the collection of information is estimated to average 1 hour per response, including the time for reviewing instructions, searching existing data sources, gathering and maintaining the data needed, and completing and reviewing the collection of information. Send comments regarding this burden estimate or any other aspect of this collection of information, including suggestions for reducing this burden, to Washington Headquarters Services, Directorate for Information Operations and Reports, 1215 Jefferson Davis Highway, Suite 1204, Arlington VA 22202-4302. Respondents should be aware that notwithstanding any other provision of law, no person shall be subject to a penalty for failing to comply with a collection of information if it does not display a currently valid OMB control number.					
1. REPORT DATE <b>1993</b>		2. REPORT TYPE		3. DATES COVERED <b>00-00-1993 to 00-00-1993</b>	
4. TITLE AND SUBTITLE <b>The Oriented Scintillation Spectrometer Experiment Instrument Description</b>				5a. CONTRACT NUMBER	
				5b. GRANT NUMBER	
				5c. PROGRAM ELEMENT NUMBER	
6. AUTHOR(S)				5d. PROJECT NUMBER	
				5e. TASK NUMBER	
				5f. WORK UNIT NUMBER	
7. PERFORMING ORGANIZATION NAME(S) AND ADDRESS(ES) <b>Naval Research Laboratory,E.O. Hulburt Center for Space Research,4555 Overlook Avenue, SW,Washington,DC,20375</b>				8. PERFORMING ORGANIZATION REPORT NUMBER	
9. SPONSORING/MONITORING AGENCY NAME(S) AND ADDRESS(ES)				10. SPONSOR/MONITOR'S ACRONYM(S)	
				11. SPONSOR/MONITOR'S REPORT NUMBER(S)	
12. DISTRIBUTION/AVAILABILITY STATEMENT <b>Approved for public release; distribution unlimited</b>					
13. SUPPLEMENTARY NOTES					
14. ABSTRACT					
15. SUBJECT TERMS					
16. SECURITY CLASSIFICATION OF:			17. LIMITATION OF ABSTRACT	18. NUMBER OF PAGES <b>67</b>	19a. NAME OF RESPONSIBLE PERSON
a. REPORT <b>unclassified</b>	b. ABSTRACT <b>unclassified</b>	c. THIS PAGE <b>unclassified</b>			

# **The Oriented Scintillation Spectrometer Experiment Instrument Description**

W. N. Johnson, R. L. Kinzer, J. D. Kurfess, M. S. Strickman

*E. O. Hulburt Center for Space Research, Naval Research Lab, Washington DC 20375*

W. R. Purcell, D. A. Grabelsky, M. P. Ulmer

*Northwestern University, Evanston, IL*

D. A. Hillis

*Ball Aerospace Systems Group, Boulder, CO*

G. V. Jung and R. A. Cameron

*Universities Space Research Association, Washington DC*

*Received: 4 August 1992; Accepted: 17 September 1992*

## **Abstract**

The Oriented Scintillation Spectrometer Experiment (OSSE) on the *Arthur Holly Compton* Gamma Ray Observatory satellite uses four actively-shielded NaI(Tl)-CsI(Na) phoswich detectors to provide gamma-ray line and continuum detection capability in the 0.05 – 10 MeV energy range. The instrument includes secondary capabilities for gamma-ray and neutron detection between 10 and 250 MeV. The detectors have  $3.8^\circ \times 11.4^\circ$  (FWHM) fields-of-view defined by tungsten collimators. Each detector has an independent, single-axis orientation system which permits offset pointing from the spacecraft Z-axis for background measurements and multi-target observations. The instrument, its calibration and performance are described.

## 1 INTRODUCTION

The Oriented Scintillation Spectrometer Experiment (OSSE) is one of four experiments on NASA's *Arthur Holly Compton* Gamma Ray Observatory (GRO) satellite. Launched on 1991 April 5, GRO has a complement of instruments which provide coordinated observations spanning six decades of energy in the gamma-ray range. OSSE has been designed to undertake comprehensive gamma-ray observations of astrophysical sources in the 0.05 to 10 MeV energy range. The instrument includes secondary capabilities for gamma-ray and neutron observations above 10 MeV that will be of particular value for solar flare studies.

OSSE follows several previous satellite instruments dedicated to investigations in the low-energy gamma-ray region, including the gamma-ray spectrometers on the HEAO-1 and HEAO-3 missions and the gamma-ray spectrometer on the Solar Maximum Mission. These instruments made pioneering observations which include the detection of diffuse positron annihilation radiation and  $^{26}\text{Al}$  emission from the galactic plane, the detection of  $^{56}\text{Co}$  emission from SN1987a, the detection of a number of galactic and extragalactic sources up to a few hundred keV, and the detection of a large number of solar flare and cosmic gamma-ray bursts.

The mission of OSSE is to extend these observations with significantly improved sensitivity. OSSE's observational program addresses a broad range of scientific objectives in the following areas:

1. Heavy element nucleosynthesis through observation of radioactivity in supernova remnants,
2. The power source in novae from observations of the associated radioactivity,
3. Binary systems containing neutron stars and black holes,
4. Pulsed and steady-state emissions from pulsars,
5. The diffuse emissions from the galactic plane and the galactic center regions and possibly the cosmic diffuse background,
6. The energy source of active galactic nuclei,
7. The intensity of low-energy cosmic rays and the matter density in the interstellar medium, and
8. Gamma-ray and neutron emissions from solar flares.

The OSSE instrument was designed to have the capabilities to address the objectives listed above by adopting a conventional scintillation spectrometer with a rectangular field-of-view (FOV), which permits mapping the diffuse emission along the galactic plane with modest angular resolution while maintaining the capability to study discrete sources. In

section 2 of this paper the instrument and its capabilities are described. Section 3 presents the GRO observation constraints and their impact on OSSE observations. In section 4 we describe the pre-flight OSSE calibration and its results, and the actual on-orbit performance of OSSE during the first year of the GRO mission is presented in section 5.

## 2 INSTRUMENT DESCRIPTION

The OSSE instrument, shown in Figure 1, consists of four identical detector systems controlled by a central electronics unit. Each of OSSE's four detectors operates, to a large degree, as an independent instrument, with separate electronic and pointing systems. The OSSE detectors are nominally co-aligned with the other pointed GRO instruments, EGRET and COMPTEL, providing coordinated gamma-ray observations of specific targets. Each of the four OSSE detectors can be independently rotated about an axis perpendicular to the nominal pointing direction of GRO to observe secondary or transient sources such as the Sun with little impact on spacecraft (S/C) orientation. The characteristics of the OSSE instrument are summarized in Table 1 and discussed below.

### 2.1 OSSE Detectors

Figure 2 displays the major components of one of the four OSSE detectors. The primary detecting element for each is a large area NaI(Tl) scintillation crystal (13-inch diameter by 4-inch thick) shielded in the rear by an optically coupled 3-inch thick CsI(Na) scintillation crystal in a "phoswich" configuration. Collimation of gamma rays and background reduction are achieved by the use of active shielding and a passive tungsten collimator. The phoswich is enclosed in an annular shield of NaI(Tl) scintillation crystals which provides anticoincidence for gamma-ray interactions in the phoswich. The annular shield also encloses a tungsten slat collimator which defines the  $3.8^\circ \times 11.4^\circ$  full-width-at-half-maximum (FWHM) gamma-ray aperture of the phoswich detector. A plastic scintillation detector covers the aperture to complete a  $4\pi$ -steradian shield for charged particle rejection. The phoswich, annular shield and associated photomultiplier tubes are completely enclosed in a mu-metal magnetic shield.

#### 2.1.1 Phoswich Detector

The phoswich is viewed from the CsI face by seven 3.5-inch photomultiplier tubes (PMTs). In this configuration, the CsI portion of the phoswich acts as anticoincidence shielding for the NaI detector. The detector event processing electronics incorporates pulse-shape analysis for the discrimination of events occurring in the NaI crystal from those occurring in the CsI by utilizing the differing scintillation decay time constants of NaI and CsI.

Table 1: OSSE Characteristics Summary

Detectors		
Type:	4 identical NaI-CsI phoswiches, actively-shielded, passively collimated	
Aperture Area (total):	2620 cm <sup>2</sup> (geometric)	
Effective Area (total):	2000 cm <sup>2</sup> at 0.511 MeV (photopeak)	
Field-of-View:	3.8° × 11.4° FWHM	
Energy Resolution:	7.8% at 0.661 MeV 3.1% <sup>a</sup> at 6.13 MeV	
Time Resolution:	4 – 32 sec in normal mode 0.125 msec in pulsar mode 4 msec in burst mode	
Experiment Sensitivities (3σ for 5 × 10 <sup>5</sup> sec)		
0.05 – 10 MeV Line γ-rays:	~ 2 – 10 × 10 <sup>-5</sup> γ cm <sup>-2</sup> s <sup>-1</sup>	
0.05 – 0.5 MeV Continuum:	~ 0.002× Crab	
Pulsars of known period:	~ 0.003× Crab Pulsar	
Gamma Ray Bursts:	1 × 10 <sup>-7</sup> erg cm <sup>-2</sup>	
Solar Flare Line γ's (10 <sup>3</sup> sec flare):	1 × 10 <sup>-3</sup> γ cm <sup>-2</sup> s <sup>-1</sup>	
Solar Flare Neutrons (> 10 MeV):	5 × 10 <sup>-3</sup> n cm <sup>-2</sup> s <sup>-1</sup>	
Pointing System		
Type:	Independent Single Axis	
Range:	192° about the S/C Y-axis	
Accuracy:	6 arc minutes	
Speed:	2°/sec (max)	
GRO – OSSE Interface		
Weight:	1820 kg	
Power:	192 watts	
Telemetry:	6492 bits/sec	

<sup>a</sup>Excluding Detector # 4. Detector # 4 has the poorest resolution at all energies, but differs significantly from the others above ~ 1 MeV.

Energy losses in the phoswich are processed by three separate and independent pulse-height and pulse-shape analysis systems covering the energy ranges: 0.05 – 1.5 MeV (*Low*), 1 – 10 MeV (*Medium*), and > 10 MeV (*High*, nominally 10 – 250 MeV). The two lower ranges are derived from the summed output of the anodes of the seven 3.5-inch PMTs (RCA 83013F). The highest range is derived from the summed output of the eighth dynodes of these PMTs. The pulse-shape discrimination in the highest range is also used to separate neutron and gamma-ray energy losses in the NaI portion of the phoswich. This discrimination uses the differing time characteristics of the secondary particles produced by these interactions (Share *et al.* 1978). Gamma-ray event validation in all three ranges includes

1. anticoincidence with energy losses in the NaI annular shield,
2. anticoincidence with aperture charged particle detector, and
3. pulse shape qualification as energy loss in the phoswich NaI crystal.

The pulse-shape analysis uses rise-time to zero-crossing time measurement on the bipolar-shaped signals from the PMTs. A time-to-amplitude converter (TAC) measures the shape of the pulses. Two amplitude discriminators operating on the TAC output define a “time window” which qualifies events as having shapes consistent with NaI energy losses and validates them for digitization. Validated events are digitized by 256-channel Wilkinson run-down analog-to-digital converters. Both pulse height (energy loss) and pulse shape (decay time) are digitized. The digitized pulse shapes are used for further event qualification in the form of energy-dependent pulse-shape discrimination. This energy-dependent discrimination permits the optimum rejection of events with partial CsI energy losses (e.g. Compton scattering) at each energy. Fully qualified events are passed on to the spectral accumulation and pulsar analysis circuits described below. The calibration and on-orbit performance of the pulse shape discrimination is addressed in section 4 (see Figures 9 and 10).

### 2.1.2 AGC System and Gain Stability

Optimum spectral resolution in the phoswich detector requires precise gain adjustment of the seven PMTs viewing the phoswich. This gain balance among the tubes is preserved in orbit by individual control of each PMT’s high voltage. The high voltage control is provided by an automatic gain control (AGC) system utilizing a light emitting diode (LED) which is optically coupled to the CsI part of the phoswich. The signal from each of the PMTs coincident with the LED flashes is compared with a reference voltage. Differences between the reference and the observed PMT signal are used to adjust the high voltage applied to that PMT. The amplitude of the LED flash is stabilized in a similar way using a PIN diode which is optically coupled to the LED assembly. This secondary control provides stable LED

output for the PMT gain measurements. The PIN diode system can also be used to change the amplitude of the LED flash, which in turn changes the gains of the seven phoswich PMTs while maintaining the gain balance for the detector. Gain increases by up to a factor of four are possible. The detectors have occasionally been operated in a  $\times 2$  gain mode when improved spectral performance at the lowest energies is desired (see section 4).

The specific task of the AGC system is to preserve the relative gain of the seven phoswich PMTs with respect to temperature and magnetic field variations. Its ability to preserve the absolute gain of the phoswich is limited by the temperature dependence of the light output from the scintillation crystals and the temperature dependence of the spectral response of the PMTs. An absolute gain stability of 0.2% per  $^{\circ}\text{C}$  has been demonstrated in calibrations (section 4). Due to the very small anticipated detector temperature variation on orbital timescales ( $< 0.1^{\circ}\text{C}$ ), the absolute gain of the OSSE phoswich is expected to be stable to within 0.1% on timescales of several hours (see section 5).

Since offset pointing is used to measure the OSSE background, the varying magnetic field orientations for the target and background pointings could produce differing gains for the measurements. The OSSE design has addressed this magnetic field sensitivity of the gain of the phoswich PMTs by incorporating, in addition to the AGC system, a double co-netic shield design. Each PMT is individually housed in a mu-metal shield; a primary continuous mu-metal shield completely encloses the phoswich, annular shield and their associated PMTs. This shielding achieves a reduction of the external magnetic field by a factor of 50 or greater at the PMTs.

The absolute gain of the phoswich is monitored and reported using an internal radioactive  $^{60}\text{Co}$  source. A  $^{60}\text{Co}$ -doped plastic scintillation detector and associated 0.75-inch PMT (RCA C83012E) is positioned within the tungsten collimator with the  $^{60}\text{Co}$  source nearest the phoswich. This configuration provides gamma-ray calibration lines at 1.17 and 1.33 MeV, and a sum peak at 2.5 MeV. By using the coincident  $\beta^{-}$  energy loss in the plastic scintillator as a calibration event tag, high signal-to-noise calibration spectra are obtained with relatively weak ( $\sim 2$  nanocurie) radioactive sources (see Figure 19). These  $^{60}\text{Co}$  calibration spectra are routinely collected in a separate data buffer and transmitted in the OSSE data.

### *2.1.3 Anticoincidence Elements*

The NaI(Tl) annular shield enclosing the phoswich is 3.35 inches thick and 13.3 inches long. It is divided into four optically-isolated quadrants or segments, each viewed by three 2-inch PMTs (RCA S83019F). Energy losses above 100 keV are detected and used for rejection of coincident energy losses in the phoswich. Three shield anticoincidence discrimination signals are used in the event processing:



Low: A 100 keV threshold (programmable from 30 - 470 keV) is used as the low level discriminator for the phoswich low and medium energy ranges,  
Med: A 1.2 MeV threshold is used as the low level discriminator for the phoswich high energy range, and  
High: An 8 MeV threshold is used as the upper level discriminator for all phoswich ranges and triggers a longer rejection pulse for possible cosmic ray overloads.

Annular shield energy losses in the 30 keV to 8 MeV range are pulse-height analyzed as part of the diagnostic calibration analysis system discussed below. The good spectral resolution of the shield segments (9 – 10% at 0.66 MeV, see section 4) permits the use of shield spectra in the study of solar flares and gamma-ray bursts. The low level discriminator event rates from the shields are processed by the OSSE central electronics for the detection of gamma-ray bursts (see below).

The annular shield also encloses the tungsten slat collimator which defines the detector's rectangular ( $3.8^\circ \times 11.4^\circ$  FWHM) field-of-view. Each collimator was machined from 13-inch diameter by 7.25-inch thick sintered ingot of tungsten alloy to form  $0.54'' \times 1.58''$  aperture cells. The tungsten slats are 0.075'' thick in the  $3.8^\circ$  direction and 0.113'' thick in the  $11.4^\circ$  direction. As discussed in section 4, the high stopping power of tungsten provides passive collimation which opens only slightly at higher energies.

The aperture of each detector is covered by a charged particle detector (CPD) to complete the  $4\pi$ -steradian charged particle rejection for the phoswich. The CPD consists of a 20-inch square by 0.25-inch thick plastic scintillator (Bicron BC408) viewed by four 2-inch PMTs (RCA S83019E). Energy losses above a nominal threshold trigger rejection of coincident energy losses in the phoswich. The threshold is controlled by command but is typically set at 40% of the energy loss of minimum ionizing protons to provide better than 99.9% particle detection efficiency.

#### *2.1.4 Detector System Deadtime*

The detector is inhibited from accepting new phoswich events during the processing of previously validated events and during time periods coincident with energy losses in the anticoincidence elements above their veto thresholds. Livetime-corrected rates in the OSSE detectors require measurement of this deadtime. Each of the three phoswich energy ranges has its own deadtime or inhibit signal which is formed from the logical "or" of the phoswich event processing signals and the veto signals from the anticoincidence elements. The configuration of anticoincidence elements contributing to each deadtime signal and their veto duration can be changed by command. Table 2 summarizes the deadtime elements and their

Table 2: Event Processing Deadtimes

Detector Element	Deadtime per event in element ( $\mu\text{sec}$ )
Phoswich	
Phoswich LLD	3.7
Phoswich ULD	30
Linear Gate	3.5
Conversion	2.5 – 11
Dig Time Window	12
Store	11
Anticoincidence <sup>a</sup>	
NaI Shield LLD	2.3 / 5
NaI Shield MLD <sup>b</sup>	2.3 / 5
NaI Shield ULD	10 / 30
CPD LLD	2.3 / 5

<sup>a</sup> Shield and CPD are command controlled to one of two veto times.

<sup>b</sup> Medium Level Discriminator,  $\sim 1.2$  MeV for phoswich high range

duration. The deadtime measurement consists of sampling the inhibit signal at a frequency of 128 kHz; a deadtime counter is incremented for each sample which indicates that the system is inhibited. The deadtime counter is transmitted in the detector housekeeping information with a time resolution of 250  $\mu\text{sec}$  which provides typical accuracy of  $\Delta T/T \sim 2 \times 10^{-5}$ .

The phoswich event processing consists of 1) amplitude qualification, 2) shape qualification, 3) conversion, 4) digital time window qualification, and 5) memory storage. The conversion is performed by a Wilkinson run-down system which has an amplitude-dependent duration. The worst case phoswich event processing time is  $\sim 42$   $\mu\text{sec}$ , but the digital time window and storage processing run independently of the qualification process. Thus the phoswich deadtime per qualified event is in the range  $\sim 10 - 18$   $\mu\text{sec}$ . Phoswich events which exceed the energy range upper level discriminator (ULD) are rejected and have a fixed deadtime of 30  $\mu\text{sec}$ . The anticoincidence elements contribute a fixed deadtime per event above threshold. The time interval is either 2.3 or 5  $\mu\text{sec}$  as selected by command. The shield upper level discriminator veto durations are 10 or 30  $\mu\text{sec}$ .

Table 3: Central Electronics Computer Summary

Processor	SBP 9989 microprocessor
	3 MHz clock
	16 interrupts
Memory	32 kilobytes Read Only Memory
	16 kilobytes Error Correcting Read/Write Memory
	38 kilobytes Data Read/Write Memory
Input/Output	2 DMA (direct memory access) Channels
	58 programmed I/O channels

## 2.2 Central Electronics

The overall operation of the OSSE instrument is controlled by the central electronics (CE) unit. The CE provides 1) the primary interface with the GRO S/C for power, command and telemetry, 2) control of the acquisition and formatting of the data from the detectors into the OSSE telemetry stream, 3) coordination of the detector pointing positions with the data collection, and 4) reaction to events such as burst triggers or anomalously high rates in the charged particle detectors to change the OSSE operating mode or to place the instrument into a standby mode during hazardous situations. These tasks are executed by a computer system in the CE which is based on a Texas Instruments 9989 microprocessor. The CE contains two of these computers, one of which is a standby spare. The properties of these computers are summarized in Table 3 and their capabilities are discussed below.

### 2.2.1 Data Processing and Telemetry Organization

The OSSE CE computer software is organized into functional tasks controlled by prioritized service interrupts. These interrupt services include

1. Telemetry Data Synchronization. OSSE is allocated approximately 6.5 kilobits per second of the GRO 32 kilobit per second telemetry stream. This allocation is provided

in the form of an OSSE telemetry “packet” of 1692 bytes which is transmitted every 2.048 seconds. The CE receives an interrupt from the S/C every 2.048 seconds which initializes the transfer of the telemetry packet to the S/C and begins the construction of the next packet. These interrupts also synchronize the OSSE data collection activities with the S/C telemetry and provide the basic timing unit for data collection intervals.

2. Event Timing. The S/C provides absolute timing capability with its Time Transfer Unit (TTU) which maintains Universal Time (UTC) to an accuracy better than 0.1 msec. OSSE uses the TTU information and its associated 1.024 MHz and 1 Hz timing signals to record the time of events with 0.125 msec resolution.
3. Command Processing. OSSE receives commands from the GRO Command and Data Handling Unit on eight serial command ports. These commands configure the detectors, the operating mode of the CE computer, or permit modification of the software executing in the CE computer.
4. Detector Command and Data Processing. The computer routes ground commands to the detectors as well as creating its own commands in support of data collection from the detectors. It preserves the complete command state of each of the detectors and restores the detectors to their operational state as required.

### *2.2.2 Positioning*

Each OSSE detector has an independent positioning system which provides 192 degrees of rotation about the spacecraft’s Y axis. As shown in Figure 3 this rotation range extends from 51 degrees beyond the +Z axis (toward the –X axis) through 141 degrees below the +Z axis in the +X direction. Stepper motors and associated gear trains provide 3.3 arc minute (18 steps/degree) positioning resolution in the operating range. Each system has a standby redundant stepper motor and a linear actuator which transfers control between the primary and redundant drives.

A detector’s position is established at calibration reference points at either end of the operational range of motion. Subsequent positioning is measured by counting steps from the reference points. A potentiometer with dual tracks and wipers is calibrated to provide backup detector location to an accuracy of 6 arc minutes. The recalibration of the positioning system at the one of the reference points is performed periodically by the CE computer in response to commands from the ground controllers.

The OSSE instrument achieves its sensitivity through offset-pointed background measurements. OSSE’s pointing control system is used to move the OSSE detector’s field-of-view

(FOV) away from a particular source target to sample the detector background. These alternating target and background measurements occur on time scales which are fast, generally 2 minutes, relative to the typical orbital background variations. The difference between the energy loss spectra while viewing the source and while viewing the backgrounds represents the spectrum of the source. Each of the detectors is controlled independently by the OSSE CE and has its own observing sequence. Nominal observing sequences will have the detector motions phased so that two of them will be viewing the source while the other two will be measuring the background.

The tungsten collimators are oriented with the  $3.8^\circ$  (FWHM) field-of-view parallel to the detector scan plane. As seen in Figure 11, a background offset of  $\sim 5^\circ$  provides significant modulation of the source contribution. This background offset, however, is programmable so that alternate background offsets can be selected in source-confused regions or for other scientific reasons. The nominal observing sequence observes the background on both sides of the source position. A polynomial fit to the sequence of background observations will generally be used in the data analysis to estimate the background during the source observation. This alternate-side technique minimizes the systematic effects of modulation of gamma-ray background local to the spacecraft. A typical detector observing sequence consists of continuous repetition of the following sequence:

1. Observe the source direction for 2 minutes,
2. Move to a background position  $\sim 5^\circ$  counter-clockwise from the source and observe for 2 minutes,
3. Return to the source direction and observe for 2 minutes, and
4. Move to a background position  $\sim 5^\circ$  clockwise from the source and observe for 2 minutes.

Detector motion occurs at a fixed rate of  $2^\circ$  per second. An observing sequence can consist of up to eight source and background offsets which can be used for source positioning or more complicated background modeling.

### *2.2.3 Secondary Source Opportunities*

The GRO observation planning process discussed in section 3 considers the targets away from the Z axis which would be accessible with OSSE's positioning capability. In particular, finding a second target at an OSSE orientation near the X-axis, in addition to the primary target at the Z-axis, provides the possibility of a secondary target which OSSE can view at times in the orbit when the primary, Z-axis, target is occulted by the earth. Thus, OSSE can make good use of the Z-axis earth occultation periods by viewing a secondary target.

By proper selection of the S/C orientation for a two week observation, OSSE can perform observations of both the primary, Z-axis, target and a secondary target during each orbit without reorientation of the S/C.

This switching between the primary and secondary viewing programs on an orbital timescale is controlled by timed commands which are stored in the S/C computer. The execution times of the commands are determined by OSSE mission planning based on the viewing angles to the two targets. A single command is required to activate one of the viewing programs. OSSE supports four different viewing programs which can be loaded by command from the ground.

The major activity of the GRO/OSSE observing program planning is finding the optimum selection of primary-secondary target pairs which provide the best use of the OSSE observing time and meet the GRO viewing constraints discussed in section 3.

#### *2.2.4 Autonomous Mode Changes*

As shown in Figure 3, OSSE is located on the +X end of the GRO spacecraft. Solar array articulation constraints and spacecraft thermal constraints require the Sun to be in the +X hemisphere. Consequently, OSSE's orientation capability often permits direct viewing of the Sun even when the other instruments are observing in some other direction. Thus, the Sun is often a candidate secondary target for OSSE viewing. As indicated in Figure 3, the OSSE orientation range and solar array range do not exactly coincide but have a  $141^\circ$  region of overlap.

This ability to select a GRO viewing program which enables OSSE to move from the Z-axis target to the Sun without re-orientation of the S/C provides a significant capability for the observation of solar flares. Additionally, the Burst and Transient Source Experiment (BATSE) on GRO has the ability to detect and identify solar flares and signal OSSE that a possible flare has begun. OSSE can react to the BATSE solar flare trigger by initiation of a new viewing program and telemetry format which moves all detectors to solar viewing.

BATSE nominally takes 3 seconds to identify the transient event as coming from the solar direction. This is done by comparison of transient event responses in the solar-viewing BATSE detectors (see Fishman *et al.* 1989). The response time to a solar flare typically would be  $\sim 60$  seconds to re-orient the detectors and requires no contact with the ground controllers.

OSSE can also react to a BATSE solar trigger by changing the data collection mode of the calibration system, to provide the capability for accumulating spectra from the OSSE annular shield segments with a time resolution of up to  $\sim 4$  seconds. This capability can

provide modest spectral and temporal resolution data on solar flares without re-orientation of the OSSE detectors.

#### *2.2.5 Charged Particle Monitors*

The OSSE instrument includes a charged particle monitor (CPM) detector which operates continuously. The high voltage to the PMTs for all other detector elements is removed during traversals of the South Atlantic Anomaly (SAA) where the high fluxes of charged particles can potentially degrade the performance and lifetime of the PMTs. The CPM is a 0.75-inch diameter plastic scintillation detector which is enclosed in a passive shield of  $\sim 3 \text{ gm cm}^{-2}$  of aluminum to reduce its sensitivity to electrons. Thus the event rates in this detector provide a monitor of the high-energy charged particle environment which causes the dominating background variations observed in OSSE. Additionally, the CE monitors the CPM rates to provide a backup detection of the S/C entry into the SAA. The S/C has primary responsibility for providing this function using absolute time commands stored in the S/C computer.

### **2.3 Thermal Control System**

The OSSE thermal control system has been designed to maintain the detector systems within the operational temperature range of  $20 \pm 5^\circ\text{C}$ . The passive thermal control system consists of a 20-layer multi-layer insulation (MLI) blanket attached to a Kevlar Nomex support structure surrounding the instrument (Figure 1). A Beta cloth exterior surface and aluminum radiators on the +Y and -Y surfaces provide the appropriate coupling to the environment.

Each detector contains an active thermal control system incorporating a proportional controller operating over the temperature range of 19 to 21 °C. Thermostatically-controlled makeup heaters are provided to protect the instrument during extended non-operating periods while in orbit. Performance of the thermal control system is detailed in section 5.

### **2.4 OSSE Data Types**

The contents and format of the OSSE telemetry packet are functions of the OSSE operating mode and telemetry format. OSSE can operate in any of 18 pre-programmed telemetry formats or can have new formats designed and uploaded from mission control into the CE memory. These telemetry formats adjust the telemetry allocation to the various OSSE data types to optimize the OSSE telemetry data for the scientific objectives of a particular GRO observation period. These formats support the various time resolutions

and event rate capabilities of the detectors' gamma-ray measurements. The four detectors operate independently, but their data acquisition tasks are synchronized by timing signals provided by the central electronics. It controls the timing of data acquisition and selects from various detector data types in its formation of the OSSE telemetry stream. These data are discussed below.

#### *2.4.1 Spectral Memory Data*

The primary data from the OSSE instrument consist of time-averaged energy loss spectra from the individual detectors. Each detector accumulates separate energy loss spectra from the validated gamma-ray events in each of the three energy ranges. The time interval (spectrum acquisition cycle time,  $T_{SAC}$ ) for these accumulations is a function of the overall operating mode of the OSSE experiment and is typically 8 or 16 seconds. The acquisition cycle time is controlled by the OSSE central electronics which selects the  $T_{SAC}$  interval based on the OSSE telemetry format. Acquisition times in the range between 4 seconds and 32 seconds are available. The detectors' accumulation memories are double buffered so that accumulation occurs in one memory while the other memory is transmitted to the telemetry formatter. The accumulation memories can support a maximum of 4095 events per spectral channel per  $T_{SAC}$ .

Gamma-ray events for the low and medium phoswich energy ranges (0.05 – 1.5 MeV and 1 – 10 MeV) are separately accumulated into 256-channel spectra. These energy-loss spectra have uniform channel widths of  $\sim 6$  keV and  $\sim 40$  keV, respectively, at nominal gain. The high phoswich energy range ( $> 10$  MeV) is pulse-shape analyzed to discriminate gamma-ray and neutron events. These gamma-ray and neutron events are then separately accumulated into 16-channel spectra. These energy-loss spectra have uniform channel widths of  $\sim 16$  MeV at nominal gain.

At the end of each  $T_{SAC}$  interval the collection process switches to the alternate accumulation buffer and the completed spectra are available for transmission to the central electronics on demand. A complete set of housekeeping data is also obtained from each detector on the  $T_{SAC}$  time scale. This includes live time and rate monitors, command state verification, analog voltages and temperature monitors.

#### *2.4.2 Pulsar*

High time resolution gamma-ray data will generally be available in the OSSE telemetry stream in one of the OSSE pulsar data modes. Validated gamma-ray events in each of the detectors are transmitted, event-by-event, to the CE pulsar processing software for inclusion



in the OSSE telemetry stream. Due to telemetry allocation limitations, the entire event stream from the detectors can not be accommodated in the OSSE packet, so the pulsar processing includes considerable event selection and compression for telemetry formatting. The pulsar processing permits the definition of up to eight energy bands to be included in the transmitted pulsar data. These energy bands, as well as the rest of the pulsar data collection configuration, can be defined in OSSE mission operations activities and uploaded into the experiment. The pulsar data can therefore be optimized to the specific observing target while limiting the event rate to that which can be handled in the OSSE telemetry.

Gamma-ray events qualified as being in one of these eight energy bands are then processed in one of two modes, “event-by-event” or “rate”, which represent different compromises in event throughput *vs* spectral and temporal resolution:

1. Event-by-event (EBE) mode, where selected events are tagged with both energy loss and arrival time. Event arrival times are recorded with 1.0 millisecond or 0.125 milliseconds resolution; these arrival times, detector identifications, and encoded energy losses are transmitted in the telemetry data. For a typical OSSE telemetry format, a maximum of  $\sim 230$  events per second can be supported in the event-by-event pulsar mode.
2. Rate mode, where high time resolution rate samples are taken in each of the eight energy bands. The pulsar rate mode can accommodate a much higher event rate than the EBE mode but at the sacrifice of spectral resolution. This mode records the number of events in each of the defined energy bands at a specified sample frequency. The highest sample rate in this mode provides a resolution of 4 milliseconds. Sample times from 4 msec to 512 msec are supported. In a typical 4-msec mode, a maximum of  $\sim 10^4$  events per second can be supported.

#### *2.4.3 Gamma-Ray Burst Data*

OSSE includes a gamma-ray burst capability which is based on the measurement of the summed gamma-ray event rates in the NaI annular shields. These event rates are sampled by the OSSE central electronics on a selectable time scale of from 4 msec to 32 msec. A gamma-ray burst trigger signal, either from BATSE or from internal processing, activates the storage of the next 4096 samples in a burst memory. A selectable fraction of this memory preserves the rate samples prior to the trigger. With coarser time resolution ( $\sim 1$  sec), rate samples from the individual NaI shield quadrants are available which can be used to identify the direction of the gamma-ray burst. Approximately 5 minutes are required to transmit the burst history in the OSSE telemetry packet.

The OSSE internal burst trigger monitors the annular shield rate samples for successive samples above a specified event rate as the indication of a gamma-ray burst. The BATSE Burst Trigger Signal is the primary burst trigger signal for OSSE since it incorporates more sophisticated trigger detection and a burst direction measurement which will be able to identify possible solar flares (Fishman *et al.* 1989). As discussed above, this ability to react to solar flares significantly enhances the OSSE science. Part of the OSSE response to a burst trigger signal permits the activation of an altered science data collection mode for the OSSE instrument which includes a change in the detector positions and/or change in the telemetry format for data collection.

#### 2.4.4 Diagnostic Data

Significant capability has been developed in the detector systems to monitor the performance of the phoswich and anticoincidence detector elements. Analysis of these data permit verification of and subsequently, by command, optimization of the performance of the various detector components. These data types include:

1.  $^{60}\text{Co}$  absolute gain calibration. As discussed above, the  $\beta$ -tagged  $^{60}\text{Co}$  events in the phoswich provide a high signal-to-noise measurement of the phoswich gain and performance. These tagged events are accumulated in dedicated  $^{60}\text{Co}$  calibration memories and transmitted to the central electronics on demand. Accumulation buffers of 256 channels are provided for both the low- and medium-energy ranges. Typical accumulation times are 2 minutes and are synchronized with detector positioning. Figure 19 shows a representative  $^{60}\text{Co}$  calibration spectrum taken in flight.
2. Anticoincidence system performance. Each of the segments of the NaI annular shield and the charged particle detector which cover the aperture contain imbedded  $^{241}\text{Am}$  calibration sources. These calibration sources consist of  $\sim 5$  nanocurie  $^{241}\text{Am}$ -doped NaI crystals which provide calibrated light flashes from the  $\alpha$ -particle interaction in the NaI crystal. A calibration pulse height analyzer, under control of the central electronics, cycles among these shield elements collecting energy loss spectra which are accumulated in a 256-channel calibration buffer. These spectra permit verification of the gain calibration of the element and the setting of the anticoincidence discrimination level, all of which can be changed by command. The calibration process in the central electronics controls the frequency and order of these spectral accumulations.
3. Pulse-shape discrimination efficiency. The ability to monitor the performance of the phoswich pulse-shape analysis provides the information required to adjust the pulse-shape discrimination levels for optimum background rejection. This information is also

required to measure the energy-dependent discrimination efficiency which is part of the instrument response model for correction of measured energy-loss spectra into incident photon spectra. On an event-by-event basis, both the digitized pulse height and digitized pulse shape are transmitted to the central electronics for additional processing. Multiplexors in the detectors select which energy ranges are transmitted to the central electronics. Each phoswich contains an  $^{241}\text{Am}$  calibration source similar to those in the shield elements which provide both pulse-shape and pulse-height references for these measurements.

The central electronics processes these data from one detector at a time, accumulating two-parameter spectra (phoswich energy loss *vs* pulse shape). These spectra are transmitted in the telemetry stream at a low rate (a typical configuration might require 20 minutes to sample the two parameter spectra from all three energy ranges from all detectors). Analysis of these spectra can produce corrections to the energy-dependent pulse-shape discrimination tables used by the detector event qualification as described above. These corrections are transferred to the instrument by command. Section 4.3.5 discusses pulse-shape discrimination performance.

### 3 GRO OBSERVATION PLANNING

#### 3.1 GRO Viewing Constraints

The GRO, shown in Figure 3, is a 3-axis stabilized spacecraft capable of positioning the Z axis any direction at any time of the year. The spacecraft attitude is, however, restricted by numerous constraints which limit the opportunities for specific OSSE field-of-view orientation and secondary target viewing and must be considered in GRO observation planning. These constraints fall into two categories: hardware constraints which must be satisfied in order to ensure the proper functioning of the spacecraft, and scientific constraints which are goals that must be achieved by the end of each phase of the mission. There are three hardware constraints of concern to the viewing program: spacecraft power, thermal and attitude determination. These constraints are depicted graphically in Figures 3b and 4 and described below.

The power constraint requires that the Sun completely illuminate both solar arrays and that the angle between the Sun and solar array normal vector remain less than a limiting value which decreases with age (about  $44^\circ$  at the beginning of life and  $28^\circ$  after 2.25 years). This constraint is equivalent to a cone of exclusion about the +Y axis in which the Sun is not allowed. The solar arrays rotate about the spacecraft Y axis to achieve the maximum array illumination for each spacecraft attitude, thus minimizing the angle between the Sun

and the array normal vector. This constraint is satisfied in the example shown in Figure 4 by ensuring that the Sun remains inside the solar constraint box during the observation.

The thermal constraint requires that the Sun is always in the spacecraft's +X hemisphere. Spacecraft thermal radiators and other sensitive hardware are directed in the  $-X$  hemisphere and cannot tolerate extended exposure to the Sun. This constraint is combined with the power constraint in Figure 4 by forming two edges of the solar constraint box (the spacecraft Y-Z plane dividing the +X and  $-X$  hemispheres).

The attitude constraint requires that at least two of the three attitude sensors on GRO can be used. These sensors are the two fixed head star trackers (FHSTs), located in the spacecraft's X-Y plane at  $\pm 45^\circ$  from the  $-X$  axis, and the fine sun sensor (FSS) with its field of view centered on the X-Z plane in the +X direction. The two FHSTs require the presence of an acceptable guide star (isolated star with magnitude  $5.7 < m < 2$ ) in their  $8^\circ \times 8^\circ$  fields of view and that the Moon is more than  $9^\circ$  from its optical axis. The FSS is, in fact, two sensors treated here as one with an enlarged field of view. Each FSS has a  $62^\circ \times 62^\circ$  square functional field of view. The optical axis of both are in the spacecraft's X-Z plane,  $30^\circ$  and  $92^\circ$  from the Z axis respectively. The FSS can be used for attitude determination if the Sun is anywhere inside the field of view. The spacecraft is operated with either 2 FHSTs or one FHST and one FSS at all times. Only one mode is operational at any time. It is not possible to switch rapidly between these two modes of operation. Either of these modes can be used in the example shown in Figure 4; the Moon never passes within  $9^\circ$  of the FHST field of view, and the Sun is always inside the FSS field of view during the entire observation.

Scientific constraints are subject to change as the mission progresses. During phase I of the mission (observations from May 1991 through November 1992), the scientific constraints require observations of generally 2-week duration which provide full sky coverage for the broad field-of-view instruments (EGRET and COMPTEL). The sequence of observations was optimized with respect to both the OSSE source priority and the COMPTEL and EGRET viewing performance statistics.

### 3.2 OSSE Target Selection

OSSE's capability of viewing two or more targets per orbit is designed to make use of the parts of each orbit when a single target would be occulted by the earth. By considering the seasonal ordering of the GRO Z axis viewing directions, OSSE can select secondary viewing directions which contain interesting targets well away from the Z axis and thereby increase the total time that either target is visible. In general, OSSE's total exposure is improved as the separation angle between the primary and secondary targets is increased.

While the positioning system provides  $192^\circ$  of rotation, all four of OSSE detectors have a completely unobstructed view of a target (including offset backgrounds) for  $\sim 90^\circ$  of this range. This range extends  $\sim 4.5^\circ$  into the  $-X$  hemisphere from the  $Z$  axis to  $\sim 85.5^\circ$  into the  $+X$  hemisphere. Beyond this range, two of the detectors partially obscure the other two. OSSE can train two detectors on a target over the full range of motion. It is sometimes desirable to make two-detector observations if the percentage of time when both the primary and secondary targets are visible is a high percentage of each orbit.

The OSSE viewing program is built from a categorized and prioritized list of targets selected on the basis of previous gamma-ray measurements or interesting characteristics in other energy ranges. Source confusion and extended regions of emission such as the galactic plane place additional constraints on the viewing plan when the orientation of the OSSE rectangular field-of-view with respect to the target region must be considered.

## 4 OSSE CALIBRATION

### 4.1 Summary

Calibration of the OSSE instrument was performed using both the flight detectors and, in somewhat more detail, the engineering model detector. The engineering model detector is a nearly exact copy of a single flight detector and was used during the calibration activities for tests in which it was not possible to use the actual flight detectors because of time or flight instrument safety constraints.

The calibration activities were separated into several phases during which different aspects of the instrument response were investigated. The primary calibration phases were designed to study the OSSE instrument response to low energy ( $0.05 - 10.0$  MeV) and medium energy ( $4 - 20$  MeV) gamma rays and to moderate energy ( $10 - 200$  MeV) neutrons and protons. During each of these tests the temperature of the detectors was precisely controlled to within  $\pm 0.1^\circ\text{C}$ .

The primary calibration effort consisted of measuring the OSSE instrument response to low energy ( $0.05 - 10.0$  MeV) mono-energetic gamma rays. These gamma rays were produced by shielded and collimated radioactive sources which provided mono-energetic photons at discrete energies over the range  $0.06 - 6.1$  MeV. A list of the radioactive sources used during these calibrations is provided in Table 4. Initial line gamma-ray calibrations were performed using the engineering model detector. During a continuous eight-month test a series of measurements was performed to provide detailed information about the electronic, energy, angular and thermal performance of an OSSE detector. Additional tests were performed to verify the operation of many of the detector subsystems and to provide recovery modes in the

Table 4: OSSE Calibration Radioactive Source List

Isotope	Major Lines (MeV)	Half Life	Source Strength
$^{22}\text{Na}^{(a)}$	0.511, 1.275	2.60 years	7 mCi
$^{57}\text{Co}$	0.122, 0.137	272 days	12 mCi
$^{60}\text{Co}$	1.173, 1.332	5.27 years	12 mCi
$^{88}\text{Y}^{(a)}$	0.898, 1.836	106 days	13 mCi
$^{113}\text{Sn}$	0.392	115 days	12 mCi
$^{137}\text{Cs}$	0.662	30.2 years	12 mCi
$^{139}\text{Ce}$	0.166	137 days	15 mCi
$^{203}\text{Hg}^{(a)}$	0.073, 0.279	46.8 days	18 mCi
$^{207}\text{Bi}$	0.072, 0.570, 1.064, 1.770	32.2 years	0.1 mCi
$^{228}\text{Th}^{(a)}$	0.082, 0.239, 0.583, 0.860, 2.614	1.91 years	10 mCi
$^{241}\text{Am}$	0.060	458 years	12 mCi
$^{241}\text{Am}/\text{Be}^{(b)}$	2.223 <sup>(c)</sup> , 4.430	458 years	96 mCi
$^{244}\text{Cm}/^{13}\text{C}^{(b)}$	6.130	20 years	800 mCi

<sup>a</sup> Sources used during angular calibrations.

<sup>b</sup> Alpha induced gamma-ray emission.

<sup>c</sup> From n-p capture.

Table 5: OSSE Van de Graff Target List

Target	Major Lines (MeV)
Fluorine	6.1, 7.0
Lithium	14.0, 17.0
Boron Carbide	4.4, 11.7, 16.1
Aluminum	10.5
Tritium	19.6

event of possible component failures such as the loss of one or more PMTs. Following these measurements, a nearly identical set of calibrations were performed during a three-month test of the OSSE flight instrument. Many of these flight-instrument calibrations were reproduced during an additional one-month test just prior to the shipment of the OSSE instrument to TRW for integration on the GRO spacecraft. Engineering model tests were performed at the Chesapeake Bay Detachment of the Naval Research Laboratory in Chesapeake Beach, Maryland, and the flight instrument tests were performed at the Ball Aerospace Systems Group facility in Boulder, Colorado.

The detector response to medium energy gamma rays was measured by exposing the engineering model detector to accelerator-generated gamma-ray lines in the energy range 4 – 20 MeV. These gamma rays were produced by bombarding selected targets with 1.5 MeV protons. Targets used and the resulting line energies are listed in Table 5. These tests were performed at the Naval Research Laboratory Van de Graaff accelerator facility in Washington, DC.

The detector response to neutrons was measured by illuminating the engineering model detector with neutron beams produced by bombarding  $^7\text{Li}$  targets with mono-energetic protons with energies between 30 and 200 MeV. The charged particle response was also measured using the scattered proton beams. These tests were performed at the Indiana University Cyclotron Facility in Bloomington, Indiana.

Detailed Monte Carlo simulations of the detector response to gamma rays have been performed to understand the full detector performance characteristics, both in energy and angle. Data accumulated during the low- and medium-energy gamma-ray calibrations were

used to validate the Monte Carlo simulation so that it could be used to extend the calibration results to configurations not studied during the calibration activities. These simulations also provided an understanding of the corrections to the calibration measurements required to estimate the detector responses to parallel incident gamma rays. Monte-Carlo simulations of the radioactive source geometry were also used to correct for effects of beam contamination due to scattering in the source holder.

An independent Monte Carlo simulation of the neutron response of these detectors was also performed. Results of this simulation, when combined with the neutron and proton calibration measurements, provide a detailed understanding of the detectors' neutron responses.

## 4.2 Calibration Description

The sources listed in Table 4 were selected to provide energy coverage with isolated gamma-ray lines over the energy range 0.06 – 6.1 MeV. Few laboratory gamma-ray line sources are available between 3 and 10 MeV; only two lines in this energy range were used for the OSSE radioactive source calibration. The absolute intensities of most of the sources listed in Table 4 were calibrated with respect to reference National Bureau of Standards sources, which provided a certified absolute accuracy of better than 5%.

The radioactive sources were placed in a source holder/collimator structure which was designed to minimize scattering and to provide a uniform collimated beam incident across the full instrument envelope. The source holder/collimator was located at a distance of 145' from the detectors, providing a nearly parallel incident beam. The position, size, uniformity, spectrum and intensity of the beams produced by the radioactive sources were mapped using two 5"  $\times$  5" NaI(Tl) crystal detectors and a Ge(Li) detector located near the instrument. These measurements and the assayed source intensities, together with Monte Carlo simulations of the source holder/collimator and the scattering in the intervening air, provided two independent measures of the absolute intensities for each of the radioactive sources. Agreement between these two determinations of the absolute intensities provided an uncertainty in the source activities of about 2% for many of the radioactive sources.

To understand and optimize the OSSE response to high-energy neutrons, calibrations of the engineering model detector were performed using neutron beams produced by the bombardment of  $^7\text{Li}$  with mono-energetic proton beams of energies 30, 55, 90, 140, and 200 MeV at the Indiana University Cyclotron. The  $^7\text{Li}(p,n)^7\text{Be}$  interaction produces a neutron spectrum with about half of the neutrons in a nearly mono-energetic peak about 1.5 MeV below the proton energy; the remainder of the neutrons are in a flat continuum extending to low energies (Byrd and Sailor 1989). Time-of-flight and coincidence timing was used to select the high-energy portion of the pulsed neutron beams. Variations of the detector response



with both energy and angle were measured.

### 4.3 Instrument Performance

#### 4.3.1 Photopeak Line Profile

High statistics data ( $\sim 10^6$  photopeak events) for the isolated gamma-ray lines permitted a study of the photopeak line profiles for the spectra from the phoswich and shield elements for each of the flight detectors. Spectral data from the phoswich elements of each detector indicate photopeak line profiles that deviate from a simple gaussian shape. The magnitude of the deviations vary from detector to detector and the effect is energy dependent. The observed photopeak line profile can best be characterized as an energy-dependent broadening of the low energy side of the photopeak. An example of the non-gaussian nature of the photopeak shape for a typical detector is shown in Figure 5. The cause of these observed deviations from the expected gaussian shapes is not well understood, although they are consistent with effects expected from observed regional non-uniformities in the large crystal volumes.

Based on careful analyses of the photopeak line profiles as a function of energy for each of the detectors, a model was constructed which represents the energy-dependent photopeak line profile for each detector. This model consists of two gaussian peaks having the same width but with different amplitudes and peak positions. The total photopeak amplitude is given by the sum of the amplitudes of the two gaussian peaks, and the photopeak energy resolution is derived from the composite of the two gaussians. The separation between the two gaussians and their relative amplitudes were determined from the calibration data for each detector. The relative amplitude of the lower-energy gaussian to the total photopeak amplitude was found to be  $\sim 15\%$ , independent of energy, with the exception of detector #4 where the amplitude of the lower-energy gaussian increases with energy to nearly 50% of the total photopeak at energies above  $\sim 2$  MeV.

A comparison of the fits to a typical photopeak line for both the double gaussian model and a model consisting of a simple single gaussian profile is shown in Figure 5. Similar continuum models were used in both cases. As can be seen, the simple single gaussian model provides an estimate of the photopeak maximum which is offset from the true maximum of the data. In addition, the shape of the data is not well described by a simple gaussian model, as shown by the residual plot in Figure 5. The double gaussian model, for which the separation and relative amplitudes of the two gaussians are fixed based on the energy of the line, fits the data well over the entire photopeak. In general, this model gives satisfactory fits at all energies for the four detectors. The double gaussian model was used to produce

all of the phoswich results discussed below.

#### *4.3.2 Photopeak Effective Area*

The photopeak effective area for a typical OSSE detector is shown in Figure 6. The data points in the figure are the measured effective areas corrected for geometry effects of the calibration configuration. The amplitude of these effects ( $\sim 4\%$ ) were determined by comparison of diverging beam and plane parallel beam Monte Carlo simulations. Small energy-dependent corrections due to source-holder beam contamination at energies below 500 keV are not included. The continuous curve represents the effective area determined by the simulation of the detectors response to an incident plane parallel beam. The scatter in the data points from the curve suggests that the absolute intensities of the radioactive sources were determined to better than the nominal five percent level shown in the figure, as discussed in section 4.2. Each of the four detectors' measured response is well represented by the Monte Carlo simulation.

#### *4.3.3 Spectral Resolution*

Figure 7 shows the measured spectral resolutions for detector #3 at nominal and twice nominal gain. Measured resolutions represent the composite FWHM of the fitted double gaussian line model. The curves represent fits to the data with a model consisting of two components, the typical gain-independent resolution function and a gain-dependent term. The latter is required because of an electronic noise signal introduced by a zener diode located in the final stage of each of the phoswich PMTs to maintain gain stability in high count-rate environments. The resolution degradation due to the effect of this unamplified noise decreases with increasing gain (increasing PMT voltage). At twice-nominal gain, the noise effect is quite small. Photopeak resolutions of the four detectors at various energies for both nominal and twice-nominal gain are given in Table 6. These data are derived from the energy resolution model fitted to the calibration data. As can be seen, both the photopeak resolutions and the magnitude of the zener diode noise effects differ from detector to detector.

#### *4.3.4 Energy Pulse-Height Analysis*

Non-linearities in the detectors' energy pulse-height analyzers (PHAs) can be separated into integral and differential components. Differential non-linearity effects produce discontinuous channel-to-channel variations, while integral non-linearity effects change the overall shape of the channel-to-energy relationship in a smooth fashion, with only small changes from one channel to the next.

Table 6: OSSE Detector FWHM Photopeak Resolution (Percent)

Energy (MeV):	0.10	0.20	0.30	0.51	0.66	2.2	4.4	6.1
Detector 1								
Nominal Gain	19.1	12.7	10.5	8.4	7.6	5.1	3.6	3.3
X2 Gain	14.8	11.3	9.9	8.3	7.6	5.1	3.6	3.3
Detector 2								
Nominal Gain	21.2	13.4	10.9	8.7	7.9	5.4	3.7	3.3
X2 Gain	16.5	11.4	9.7	8.2	7.6	5.4	3.7	3.3
Detector 3								
Nominal Gain	18.8	12.2	9.9	7.9	7.1	4.7	3.0	2.7
X2 Gain	14.7	10.4	8.9	7.4	6.9	4.7	3.0	2.7
Detector 4								
Nominal Gain	19.3	12.7	10.7	9.1	8.6	7.1	6.1	5.3
X2 Gain	14.6	10.6	9.3	8.4	8.2	7.1	6.1	5.3

Differential non-linearity effects are caused by small electronic noise in the PHA analog-to-digital converters. These non-uniformities typically result in variations in the channel widths of less than  $\sim 1.5\%$ , and systematically affect only two adjacent channels out of every 32. The differential non-linearity for the phoswich low and medium ranges of each detector were accurately measured by using precision pulse generators. Each energy range for each detector requires a different correction because each has a unique pulse-height analyzer.

After correction for differential non-linearity, the remaining integral non-linearity produces a smooth, energy-dependent, variation in the channel widths. The dominant gain-independent source of this effect is the non-linearity of the specific light output of NaI(Tl) crystals as a function of photon energy. Other non-linearity sources, which can be detector and gain-dependent, include integral non-linearities in the PHA electronics and in the PMT's. Because each phoswich PMT was carefully measured prior to instrument assembly to assure that it had no measurable non-linearity, only a small portion of the integral non-linearity can be ascribed to the PMTs. If non-linearities of the electronics are ignored, deviations from a linear channel-energy relationship can be interpreted as measuring the differential of the specific light output of the phoswich NaI(Tl) crystals. Deviation in channel width, normalized to the value at 0.662 MeV, is shown in Figure 8 for each of the four detectors. Specific light output energy dependences derived from these curves are in reasonable agreement with previous measurements (e.g. Hill and Collinson 1966).

#### 4.3.5 *Pulse Shape Discrimination*

Pulse shape analysis of events in the phoswich detector provides the discrimination between events in the NaI crystal and events in the CsI crystal. This discrimination functions as both collimation, rejecting events from the rear hemisphere of the detector, and as compton suppression, rejecting scattered events. As discussed in section 2, this shape discrimination detects the differing scintillation decay times of the two crystals. The shape measurements are affected by the same light collection and photoelectron counting statistics which affect the pulse amplitude or energy measurements, and consequently, the pulse shape discrimination (PSD) performance has significant energy dependence, particularly at low energies. Figure 9 shows a typical distribution of events in the phoswich *vs* pulse shape for NaI energies losses in the 200 – 250 keV range. Full energy losses in NaI or CsI produce approximately gaussian distributions centered on shape channels 75 and 180, respectively. Events which deposit energy in both crystals fill the region between the two gaussians. The widths of the gaussians are largely determined by the photoelectron counting statistics and broaden dramatically at low energies where system noise also contributes. A measure of the performance of the pulse shape discrimination can be specified as a figure of merit (FOM) which is defined as the separation of the two gaussians divided by the sum of their full widths

Table 7: Pulse Shape Discriminator Efficiencies

Energy (MeV)	PSD Efficiency
0.06	0.69
0.10	0.89
0.15	0.97
0.20	0.99

at half maximum. For the OSSE detectors, typical FOMs are  $\gtrsim 1.7$  at 0.122 keV,  $\gtrsim 4.5$  at 0.662 MeV and  $\gtrsim 8.5$  at 2.6 MeV.

OSSE includes energy-dependent shape discrimination which optimizes the NaI acceptance window as a function of energy. Each of the three phoswich energy ranges is divided into 16 energy bands for which ground commands define digital time windows (DTW) of acceptance. The diagnostic two parameter spectra (section 2.4.4) permit monitoring and adjustment of the DTWs for best performance in orbit. Figure 10 shows an example of a two parameter spectrum collected in orbit. This low range data displays the relative number of events at a given shape and energy as a gray level. The shape distribution at each energy has been normalized to the peak rate in the NaI gaussian to remove spectral rate dependence. Only the pulse shape region centered on the NaI distribution is displayed. At low energies the edge of the CsI distribution is evident at high pulse shape channels. Contours drawn at 0.1, 0.2, 0.5 and 1.0 times the peak level in the NaI distribution clearly indicate the broadening of the NaI gaussian distribution at low energies. At the lowest energies, the separation of NaI and CsI events is incomplete. A typical setting of the digital time windows for valid event acceptance is displayed in the figure by the two thick lines on either side of the NaI peak. Events with shape measurements falling within the thick lines for the measured energy are accepted as valid.

The effectiveness of the pulse shape analysis in separating the NaI events from the CsI events and the percentage of the NaI events within the defined DTWs become factors in the overall response function of the OSSE detectors. The energy dependence of this efficiency is shown in Table 7, which is derived from calibration data with DTW settings similar to those used in flight (Figure 10). Above  $\sim 0.2$  MeV the efficiency is essentially unity.

#### 4.3.6 Angular Response

The fields-of-view of the OSSE detectors are defined by tungsten slat collimators, as shown in Figure 2. Below several hundred keV the angular response is described well by the geometrical aperture of the collimator. At higher energies some transmission of off-axis gamma radiation through the collimator slats results in side lobes in the angular response. At large angles from the collimator axis and at energies above several hundred keV, gamma rays can also penetrate the anticoincidence shielding, with the degree of transmission increasing with higher energies.

The angular response of the OSSE detectors was determined with an extensive calibration program using the OSSE flight instrument and the engineering model detector. These tests included measuring the detector  $4\pi$  angular response at over 2000 angular positions for the engineering model detector and at nearly 400 angular positions for the flight instrument. The radioactive sources used during the angular calibration tests (see Table 4) provided measurements of the instrument angular response at energies between 0.073 and 2.614 MeV. The measured photopeak effective areas at 0.511 and 1.836 MeV are shown in Figures 11 and 12 for a typical detector. These data show the narrow field-of-view defined by the collimator, but also indicate side lobes in the response which increase in amplitude with energy and become significant at energies above  $\sim 1$  MeV. A more detailed description of the OSSE angular calibration can be found in Purcell (1988).

#### 4.3.7 Thermal Effects

The nominal operating temperature of the OSSE detectors is 20 °C, with an operational range of 15 to 25 °C. Because the detector subsystems have temperature-dependent components, many of the calibration activities described above were repeated at temperatures covering the range 12 – 27 °C. During calibration, control of the detector temperatures was achieved by placing the OSSE instrument in a thermally-controlled enclosure which provided the ability to adjust and maintain the detector temperature to within  $\pm 0.1$  °C throughout this range.

Because the AGC system tends to compensate for many thermal effects, tests were performed both with and without the AGC system active. With the electronic configuration unchanged, these two tests together show the effect of temperature on both the AGC system and on the detector performance. These data indicate that a change of  $\sim 15$  °C results in a smooth energy-dependent gain change for the detectors of only  $\sim 2 - 3\%$  when the AGC system is active. With the AGC system off, the corresponding gain change is  $\sim 4 - 6\%$ . Because the detector temperatures in orbit are stable over a two-week observation to

within  $\pm 0.1$  °C, temperature-dependent gain changes are negligible for OSSE. Temperature effects on detector resolution are found to be negligibly small over the temperature range investigated.

#### 4.3.8 Shield Element Performance

Each OSSE detector is surrounded by an annular shield composed of four segments of NaI(Tl), as shown in Figure 2. Each segment is a quarter of an annulus with an internal diameter of 13.5", a thickness of 3.35", and a height of 13.3". These segments are oriented so that two of the sectors are centered on the rotation axis of each detector and the other two are bisected by the detector's scan plane. The better-quality shield crystals are located in the optimum locations for making astrophysical observations with individual shield sectors. These elements provide active collimation of the phoswich detectors and suppression of aperture events which scatter in the phoswich and deposit energy in the shields. As collimators, the shields are essentially opaque to gamma rays below  $\sim 300$  keV. At higher energies the shielding efficiency decreases slightly with increasing energy, becoming for example, 97% at 0.5 MeV, 87% at 1.3 MeV and 76% at 2.6 MeV.

Photopeak line profiles in the shield elements are well fitted using a simple gaussian model. Figure 13 shows the resolution of a typical shield element as a function of energy for photons incident along the detector viewing axis. Performance at low energies is degraded because of the 40 keV wide energy channels. Shield element resolutions are typically 10% at 0.662 MeV, with only two elements being significantly worse than this. Because the shield elements do not have individual PMT gain control systems, resolutions of the shield elements are expected to degrade with time in orbit due to the divergence of the individual gains of the three PMTs on each shield element as they age. Eleven shield sectors degraded by less than four percent (fractionally) from calibration through the first year in orbit. The remaining shields degraded by as much as 20 percent. These generally small degradations in resolution are consistent with the observed zero to 12 percent decrease in the gains for the 16 shield elements during the first year in orbit.

#### 4.3.9 Neutron Response

Neutron and gamma-ray energy losses are differentiated by the OSSE electronics using pulse-shape discrimination in the phoswich detectors. Analyses of the neutron exposures with this procedure show that the detectors have a rather isotropic neutron response from 30 to 200 MeV, as shown in Figure 14 (Jenkins *et al.* 1991). The details of the OSSE neutron response will be addressed in a future publication.

#### 4.4 Instrument Response Model

The instrument response model describes the response of the OSSE detectors to incident gamma-rays of a given energy from a given direction. The instrument response includes the absorption of photons in material surrounding the detector, the probability of energy deposition in various detector components, the probability of an event being accepted by various instrument thresholds and the pulse-shape discrimination system, the broadening of monoenergetic features due to the finite detector energy resolution, and the pulse-height output expected given the amount of energy deposited in the detector. The instrument response is used to deconvolve these effects from the data, producing an estimate of the incident photon spectrum.

The OSSE instrument response model is derived from both gamma-ray line source calibrations described above and Monte Carlo simulations of the response of the instrument to gamma-ray lines. The simulations treat the instrument geometry and photon interaction physics in great detail and should, in principle, provide an accurate measure of the efficiency of the detector for incident gamma-rays of any energy and incident angle. However, they do not model the detector energy resolution, line shape, or the pulse-shape discrimination system. These effects vary slightly for each detector and must be determined from the calibrations.

Because it can provide information at any incident photon energy and incident angle, the simulation is used to compute the instrument response for data analysis. Monte Carlo results are modified to account for the above-mentioned phenomena that are not modeled. The calibration measurements have been used to verify the accuracy of the resulting response. In order to perform this comparison, a point gamma-ray source at the same distance from the detector as that used in calibration has been simulated. The results have been corrected for the intervening atmosphere and materials used in the instrument thermal enclosure. Contamination of the calibration beam by backscattered photons from the gamma-ray source holder has been quantified by examination of the beam using a pair of  $5'' \times 5''$  NaI(Tl) crystals. The effects of source holder contamination have been included in the calibration-simulation comparison. The  $5'' \times 5''$  studies have also supplied an absolute beam intensity calibration. Hence, no free scaling parameter is required to compare calibrations and simulations. As shown in Figure 6, there is good agreement between the simulation and the calibration measurements.

The instrument simulation models both events depositing all their energy in the NaI detector ("photopeak events") and events depositing part of their energy in the NaI detector, but not triggering an anticoincidence signal ("Compton continuum events"). The ratio of the probability of an event being a photopeak event to the probability of it being in the



Table 8: Photopeak to Compton continuum ratio

Energy (MeV)	Ratio
0.20	11.2
0.50	9.0
1.00	6.1
2.00	3.0
5.00	1.3

Compton continuum is given in Table 8 for several incident energies.

We have investigated how errors in our understanding of the Compton continuum probability affect our ability to determine the shape of incident power-law spectra of varying hardness. An error in response model continuum probability as large as 10% of the modeled OSSE response produces errors in the derived power law index of 1.3% for a hard (index of -1.5) power law or 0.1% for a soft (index of -3.5) power law. Thus, OSSE is relatively insensitive to possible Compton continuum errors within the Monte Carlo simulations and calibration measurements.

## 5 ON-ORBIT PERFORMANCE AND SENSITIVITIES

Prior to launch, two important performance aspects of the OSSE instrument – on-orbit background levels and their variability, and on-orbit detector gain stability – were not well known. Due to the background-dominated nature of OSSE observations, these phenomena are critical to obtaining realistic estimates of sensitivity. The first year of on-orbit operations have given us a sufficient understanding of instrument background and stability to perform these estimates.

### 5.1 Observed On-orbit Background

Initial estimates of OSSE background were derived from previous similar orbiting detectors (HEAO A-4, SMM/GRS), a balloon flight of the OSSE engineering model detector, and semi-empirical calculations (Dyer *et al.* 1989). Although these estimates were expected to be accurate to within a factor of two, the only estimates of the magnitude of background variability were from previous orbiting detectors with different instrument, spacecraft and orientation configurations (e.g. SMM). Since OSSE data analysis depends on estimating

the background during a source observation from backgrounds measured before and after that observation, knowledge of the variation of the background with respect to time, orbital and detector parameters is a concern. Some of the most important parameters affecting the detector background levels are magnetic cutoff rigidity, history of previous South Atlantic Anomaly (SAA) passages, position of the detector field-of-view relative to the earth's atmosphere, and position of the detectors relative to mass concentrations on the spacecraft.

Figure 15 shows how OSSE background rates vary as a function of time over a 24-hour period. Each rate history covers a different energy band. Gaps in the histories correspond to times when the instrument high voltage is turned off while the spacecraft transits the SAA. The top-most history shows magnetic cutoff rigidity on the same time scale. Note that at lower energies the SAA produces the largest background variations. This is due in large part to the  $^{128}\text{I}$   $\beta^-$  decay discussed below. Careful examination shows rigidity-related effects as well. At energies above the  $^{128}\text{I}$   $\beta^-$  endpoint energy of 2.1 MeV, effects related to magnetic rigidity and the associated modulation of the cosmic-ray induced backgrounds dominate. The instrument deadtime measured on orbit is linked to charged particle and gamma ray background and, consequently, exhibits the same orbital variability. The observed deadtime is dependent on phoswich detector and anticoincidence element rates, as described in section 2.1.4. The one-day average deadtime one year after launch is  $\sim 12\%$  in the low range,  $\sim 8\%$  in the medium range and  $\sim 5\%$  in the high range. Some of the daily averaged rates relevant to the deadtime are listed in Table 9.

Sporadic transient increases in event rate in the 0.05 – 0.10 MeV energy range have been observed. These are believed to be associated with the very high energy losses in the phoswich crystal following passage of a high-Z cosmic ray. Examples of such transients are evident in the rates shown in Figure 15, in which several large increases in the 0.05 – 0.10 MeV rate are clearly seen well above statistical fluctuations. In some instances, this increased rate has also been observed above 0.10 MeV. These increased rates are thought to be associated with the large increase in phosphorescent light in NaI(Tl) and CsI(Na) scintillation detectors following an extremely large energy deposition (Johnson *et al.* 1976). About 9% of the light emitted in NaI(Tl) is associated with a phosphorescent state with a lifetime of about 150 msec (Koićki *et al.* 1973). The instantaneous light due to this phosphorescent state is down by a factor of  $10^5$  to  $10^6$  from the 0.25  $\mu\text{sec}$  luminescent state. However, it is possible for a high-Z cosmic ray (*e.g.* Fe) to deposit  $> 10^5$  MeV in the phoswich. When this occurs, the statistical fluctuations in the phosphorescent emission simulate low-energy events for tens of milliseconds following such a cosmic-ray energy loss. These durations exceed the anticoincidence veto interval associated with the originating cosmic ray interaction. High-time resolution data indicate that the typical duration of the transient events observed in our data is a few tens of milliseconds. These typically occur 50 – 100 times per day in

Table 9: Daily Average Detector Rates

Detector Element	Rate (cnts s <sup>-1</sup> )
Phoswich	
Low Range LLD	4400
Low Range ULD	2500
Med. Range LLD	2700
Med. Range ULD	670
High Range LLD	2200
High Range ULD	240
Anticoincidence	
Shield LLD	10000
Shield MLD	2200
Shield ULD	1200
CPD LLD	240

each detector, consistent with the flux of cosmic ray Fe nuclei which dominate the number distribution of very heavy cosmic rays at the relevant energies. Data screening eliminates data affected by these events from the spectral summations on the cosmic gamma-ray sources under study. The total amount of time lost for data below about 0.20 MeV is less than 2% and does not have a significant impact on the OSSE limiting sensitivity.

Figure 16 shows two measured OSSE background spectra from 0.1 MeV to 10 MeV. The spectra consist of samples measured throughout day 11 of 1992, selected such that one of the spectra reflects times greater than 5400 seconds (roughly one orbit) since the last SAA passage and the other reflects times less than 5400 seconds. The dominant background feature resulting from an SAA exposure is the beta decay continuum from <sup>128</sup>I produced by the capture of secondary neutrons (produced by trapped protons) with <sup>127</sup>I in the NaI detector. The half-life of <sup>128</sup>I is 25 minutes, so the background measured more than 5400 seconds (one orbit) after an SAA passage shows a reduced <sup>128</sup>I contribution at energies below the beta endpoint of 2.1 MeV. Some of the prominent background features associated with cosmic-ray and SAA proton interactions and their products include 0.191 MeV from <sup>123</sup>I, a complex of lines near 0.25 MeV including <sup>121</sup>I (0.244 MeV) and <sup>123m</sup>Te (0.247 MeV), a complex of lines in the 0.6 – 0.7 MeV range including <sup>124</sup>I (0.634 MeV) and <sup>126</sup>I (0.698 MeV). The line at 6.8 MeV is associated with neutron capture by <sup>127</sup>I. The atmospheric gamma ray lines from <sup>14</sup>N (4.4 MeV) and <sup>16</sup>O (6.1 MeV) are seen to be minor contributors.

A detailed analysis of the OSSE background shall appear in a separate paper.

## 5.2 Background Estimation

Typical OSSE observations comprise a standard series of two-minute source observations alternated with two-minute background observations, with the background field directions alternating about the source direction by plus or minus five degrees in scan angle (See section 2.2.2). The series of background observations is used to estimate the background contribution from the source observations so that the source flux can be extracted. No discernable differences have been found between backgrounds at the two different offset directions in source-free regions, so that background-subtraction analyses can treat the two offsets as identical unless a confusing source is located in one background field. Sources in confusing locations have customized background offset directions.

Two background-estimation procedures are in use. The primary method used for most OSSE discrete source analyses uses no prior knowledge of the background's dependence on orbital environment parameters; it makes use only of the measured background series to interpolate in time to the source observation. The second procedure uses all background measurements made during the life of OSSE to obtain the dependence of the detector background on all relevant orbital, detector, and environmental parameters. The resulting predictive algorithm provides an estimate of the background for any source observation given only the measured parameters at that time. This procedure can make either absolute background predictions for observations where no useful background measurements are present, or background estimates by environmental parameter interpolation based on normalization to contiguous background measurements. This background-estimation procedure, which is in the developmental stage, will be used principally in confused regions where useful contiguous background measurements cannot be obtained.

In the primary background estimation procedure, a channel-by-channel prediction of the background during each two-minute source observation is obtained by interpolation from the neighboring time-sequential series of background measurements. A variety of techniques have been investigated to optimize the accuracy of the background interpolations to source times. These include simple two-point interpolation, three point interpolation with a quadratic polynomial or a cubic spline, and four-or-more-point fitting with a quadratic polynomial or a cubic spline interpolation. The limited statistical precision of the two-minute spectra and the time scale of the background variability (see Figure 15) determine the optimum subtraction procedure. The two-point interpolation procedure was found to be inadequate in some circumstances, but differences among procedures using three or more background points were small. The most successful approach, as determined by the similarity of a null

spectrum and the background-subtracted source spectrum summed from a series of two-week blank-sky or weak-source observations, requires at least one background before and after each source observation, and uses four background intervals fit with a quadratic polynomial. At time gaps in the data, three point quadratic interpolation is used before and after the gap; no interpolation across time gaps is done. This procedure gives background-subtracted spectra for blank-sky observations which are statistically indistinguishable from a null spectrum. Figure 17 shows the background-subtracted spectra resulting from a two-week observation of the region of sky containing the starburst galaxy, M82. Data from all four detectors have been added together. The error bars indicate  $1\sigma$  statistical uncertainties. The spectra are consistent with a null result.

After background subtraction is completed, comparisons of time-integrated source spectra for different ranges of relevant environmental parameters provide the means for determining whether the background-subtracted source spectra are free of incorrect background subtraction effects, and for obtaining the optimum spectrum.

### 5.3 Instrument Temperature Stability

The temperature profile of the OSSE detectors is quite stable. Typically, detector temperatures do not vary by more than  $0.1^\circ\text{C}$  on orbital time scales, due to the instrument thermal shielding and the large thermal mass of the detectors. Depending on the change in solar aspect from one spacecraft orientation to the next, some temperature variation may be observed for the first day or two after a spacecraft maneuver as the detectors come to equilibrium in the new solar configuration.

Figure 18a displays the temperature history for detector 4 during the transition from viewing period 4 to period 5, the latter being a near-worst-case cold configuration. A temperature drop of about  $0.5^\circ\text{C}$  was observed over the first day of the new configuration. After this period, the temperature stabilized at the new colder value. The standard deviation of temperature after stabilization was less than  $0.04^\circ\text{C}$ , which is typical for OSSE observations.

### 5.4 Instrument Gain Performance

The absolute gain of the phoswich detectors is determined by the internal  $^{60}\text{Co}$  calibration system as indicated in section 2. An example in-flight calibration spectrum is shown in Figure 19. Detector gain can be influenced by the magnetic field vector at the photomultiplier tubes and also the detector and photomultiplier temperatures. The observed gain is expected to be relatively independent of magnetic influence due to extensive magnetic shielding around the photomultipliers and the action of the automatic gain control system.

Examination of several representative days of data from the internal  $^{60}\text{Co}$  calibration source shows no evidence of statistically significant gain variations correlated with either orbital magnetic field variations or detector position relative to the spacecraft. During a period of constant temperature, the measured standard deviation of the gain averaged for the four detectors over a four-day period is 0.06% for variation time scales greater than 1000 seconds.

Comparisons of the measured pre-launch and post-launch gains of the phoswich detectors using the internal  $^{60}\text{Co}$  sources provide a measure of the change in gain as a result of the change in environment from calibration to orbit, as well as any launch-induced effects on the electronics or detectors. Changes were found to be less than 5%. This indicates only minor variations as a result of the launch and due to the in-orbit environment.

Variation of gain with temperature is well established, especially during the transition to the cold-case spacecraft orientation noted above. Figure 18b shows the 1.332 MeV  $^{60}\text{Co}$  calibration line centroid as a function of time for detector 4 during the same period as the temperatures in Figure 18a. The temperature change of 0.5 °C results in a gain change of approximately  $-0.3\%$  or a rate of change of  $-0.6\%/^{\circ}\text{C}$ . This is significantly higher than the rate of change measured during calibration (see section 4.3.7), but is consistent with gain change rates measured in flight for the other detectors. This discrepancy is probably due to differences in instrument thermal coupling in the calibration and space environments.

## 5.5 Spectral Resolution

Comparisons of pre- and post-launch values for these data provide an accurate measure of the relative changes in resolution for each detector. These measurements indicate a small fractional degradation in resolution of between 1% and 6% of the calibration resolution values (see Table 6). The degraded resolution is due to  $\sim 100$  times increase in background in the intense orbital cosmic ray environment. The OSSE data analysis system includes a function which provides the resolution of each detector at a given gain.

## 5.6 Gamma-Ray Line and Continuum Sensitivity

Figures 20 and 21 display continuum and line emission  $3\sigma$  sensitivity for a typical two-week OSSE observation consisting of  $5 \times 10^5$  seconds of source plus background live time per detector for four detectors. Live time is equally divided between source and background pointings. The factor of two between total observation interval and live time takes source occultation and  $\sim 12\%$  observing time loss due to South Atlantic Anomaly passages into account. Since late March 1992, spacecraft tape recorder malfunctions have reduced the fraction of data recovered from near 100% to 60 – 65%. Sensitivity has been maintained by

increasing observation duration (and, hence, reducing the number of observations) to keep live times at  $\sim 5 \times 10^5$  seconds per observation. Analysis to date indicates that limiting sensitivities are dominated by counting statistics.

## 5.7 Pulsar Detection Sensitivity

OSSE data analysis procedures currently search for pulsars using two techniques. If the period is well known, epoch folding at the known period is used to extract light curves over various energy bands. The sensitivity for pulsar detection using this technique is dependent on the duty cycle of the pulsations. Ulmer *et al.* (1991) discuss the derivation of sensitivity for square wave pulse light curves. Using their results, the pulsar sensitivity can be derived from the continuum sensitivity displayed in Figure 20 by multiplying by the factor  $\sqrt{\frac{\beta}{1-\beta}}$  where  $\beta$  is the pulse duty cycle. The sensitivity so derived assumes two detectors staring at the source for  $5 \times 10^5$  seconds. Fast pulsars such as the Crab are not very susceptible to background subtraction systematics because source modulation, and hence background measurement, occurs at the pulsar frequency.

If the pulsar period is not well known, Fourier transform techniques are used for pulsar detection and period characterization. With current computational capabilities at NRL, approximately one orbit of OSSE data, at 1/8th-millisecond time resolution, can be transformed at a time. Searches for weak periodic signals in data spanning more than one GRO orbit are complicated by two factors: instrumental background variations are strongly periodic on a range of time scales, and the data are sparse, with both random dropouts and periodic gaps from source occultation and the peculiarities of data collection. The periodic background variations introduce strong signals that can mask or be confused with celestial signals, and the sparseness of the data can spread the background power to frequencies well separated from their true values (a phenomenon known as “spectral leakage”), again masking or confusing celestial signals.

The sensitivity of such searches will depend on the details of the analysis technique (e.g., how the technique treats data gaps), so a general expression cannot be given. The simplest technique is an incoherent summation of single-orbit power spectra, which improves the sensitivity by approximately the square root of the number of orbits summed. The  $3\sigma$  sensitivity of this technique for an isolated pulsar of unknown period (less than 1 second) for an observation of  $5 \times 10^5$ -second livetime with two detectors is  $\lesssim 100$  milli-Crab pulsars in the 0.065 – 0.210 MeV energy band.

## 5.8 Solar Flare Sensitivity

In general, line and continuum sensitivities for solar flares may be derived from the curves in Figures 20 and 21, scaling by the square root of the ratio of live times. During the interval 1991 May 31 – June 15, OSSE observed a number of very strong solar flares. Peak counting rates in the OSSE detectors during these flares were high enough to result in very high dead times and significant pulse pile-up effects. These phenomena cause significant but not yet quantitatively characterized systematic effects that influence our ability to specify line parameters during the most intense phases of strong solar flares. Hence, any line sensitivity values obtained from scaling the sensitivities displayed in Figure 20 must be taken as lower limits to the actual minimum detectable flux for strong flares. Specific instrument configurations such as offset-pointed detectors from the sun are used to provide OSSE sensitivity above 1 MeV during the peak period of intense flares.

### *Acknowledgements*

The Oriented Scintillation Spectrometer Experiment represents the efforts of hundreds of people who were associated with its design, fabrication, test and calibration; these efforts are gratefully acknowledged. OSSE was designed, fabricated and tested by Ball Aerospace Systems Group, Boulder, Colorado. The OSSE team especially recognize the years of hard work and dedication to the OSSE program by the following BASG personnel: J. Conlan, S. Henninger, W. Hermanson, S. Koby, R. Letieri, R. Novaria, J. Orbock, R. Ordonez, R. Pearson and S. Varlese. The OSSE scintillation detector crystals were designed and fabricated by Bicron Corp., Newbury, Ohio, under the leadership of P. Parkhurst and J. White. We also wish to acknowledge the work of G. Mataraza and D. Krus of Harshaw, Solon, Ohio, who provided the phoswich crystals. F. Helvy of RCA provided invaluable help in the design and testing of the OSSE photomultiplier tubes.

The OSSE project at NRL was managed by G. Kowalski, and supported by P. Sandora, project secretary. E. Simson, L. Marlin, and D. Saulnier of NRL provided critical support to the testing and calibration of OSSE. The calibration at the Indiana University Cyclotron Facility was coordinated by C. Foster and D. Friesel of IUCF. The OSSE computer systems for assembly, test, and operation of the OSSE instrument were designed and developed by Software Technology Inc., Melbourne, Florida; we are particularly appreciative of the support of J. Daily, B. Leas, T. Roberts, D. Kuo, D. Wagner and B. Brownstein.

The support and leadership provided by J. Cooley, M. Davis, J. Hrastar, J. Madden and A. Peterson of the GRO Project Office at NASA's Goddard Space Flight Center and by R. Cline and J. Poppa from TRW Space and Technology Group (the mission contractor) were invaluable in the successful execution of the OSSE project.



This work was supported under NASA grant DPR S-10987C.

## REFERENCES

- Byrd, R.C. and Sailor, W.C. 1989, Nuclear Instruments and Methods in Physics Research, A274, 494
- Dyer, C.S., Truscott, P.R., Sims, A.J., Comber, C. and Hammond, N.D.A. 1989, in: Proceedings of the Gamma Ray Observatory Science Workshop, Goddard Space Flight Center, Greenbelt, MD, ed. W. N. Johnson, 4-521
- Fishman, G.J., *et al.* 1989, in: Proceedings of the Gamma Ray Observatory Science Workshop, Goddard Space Flight Center, Greenbelt, MD, ed. W. N. Johnson, 2-39
- Hill, R. and Collinson, A.J.L. 1966, Brit. J. Appl. Phys., 17, 1377
- Jenkins, T.L., Frye, G.M., Stansfield, S., *et al.* 1991, Proceedings of the 22nd ICRC, Dublin, Ireland, SH 11.1
- Johnson, W.N., Kurfess, J.D. and Bleach, R.D. 1976, Ap&SS, 42, 35
- Koički, S., Koički, A. and Ajdačić, V. 1973, Nuclear Instruments and Methods, 108, 297
- Purcell, W.R. 1988, Ph. D. thesis, Northwestern Univ., Evanston, IL
- Share, G.H., Kurfess, J.D. and Theus, R.B. 1978, Nuclear Instruments and Methods, 148, 531
- Ulmer, M.P., Purcell, W.R., Wheaton, W.A., and Mahoney, W.A. 1991, ApJ, 369, 485

## Figure Captions

Figure 1. The OSSE general configuration. The exterior thermal shield and support structure have been removed in this view and are indicated in outline.

Figure 2. The configuration of one of the four identical OSSE Detectors. The primary phoswich crystal is enclosed in a NaI annular shield made in four segments. The aperture is defined by a tungsten slat collimator. Support electronics, low voltage power supply (LVPS) and twelve high voltage power supplies (HVPS) are mounted on the sides of the assembly.

Figure 3. The Gamma Ray Observatory configuration. a) The general configuration of GRO with coordinate system axes labeled. OSSE is mounted on the +X end of the S/C. b) The constraints on GRO's attitude with respect to the sun. The solar-exclusion cone at the end of 2 years of operation is expected to be  $62^\circ$ ; during the first year, this angle was  $46^\circ$ . c) The relationship between OSSE's range of motion and the allowed solar angles.

Figure 4. Example of an attitude determined by the location of the GRO S/C's X and Z axes in the celestial sphere, which satisfy the spacecraft hardware constraints for a 2-week observing period beginning 1991 Oct. 3. This configuration supports OSSE observations of 3C 273 at the Z axis and the galactic center near the X axis. The small ovals approximate the OSSE 20%-response fields of view. The region within the solar constraint is shaded. The field of view of the fine sun sensors (FSS) is hatched. The fixed head star trackers (FHST) fields of view and Moon exclusion circles are depicted. The locus of Sun (thick line) and Moon (dot-dash line) positions during this observation are plotted as arcs.

Figure 5. A background-subtracted spectrum of the 662 keV line from  $^{137}\text{Cs}$  for detector #2 during calibration. The solid curve represents the best fit to the spectrum using the derived double gaussian model. The dashed curve represents the best fit to the spectrum using a single gaussian model. The lower panel shows the residuals between the data and each of the fitted functions in units of standard deviations.

Figure 6. Measured effective area of a typical detector for parallel beams of photons incident along the collimator axis. Corrections for diverging beam effects of  $\sim 4\%$  have been applied. The continuous curve shows the effective area determined by the Monte Carlo simulation.

Figure 7. Photopeak FWHM resolution for detector #3 at nominal gain and at two times nominal gain. At  $2\times$  gain, the instrument operates in the 0.04 – 5 MeV range.

Figure 8. Differential light output for the phoswich NaI detectors normalized at 0.662 MeV.

Figure 9. The distribution of events in the phoswich *vs* pulse shape or relative decay time. Events in the energy range 200 – 250 keV are displayed. Events in the NaI and CsI have approximately gaussian distributions well separated from each other. The widths of the distributions varies with event energy (see text).

Figure 10. The distribution of phoswich events as a function of both pulse shape and pulse amplitude or energy loss. Only the pulse shape region centered on the NaI distribution is displayed for the low energy range. The shape distribution at each energy has been normalized to the peak rate in the NaI gaussian to remove spectral rate dependence. Logarithmic contours quantify the trends in the distribution. The thick stair-step lines on either side of the NaI distribution define typical energy-dependent event acceptance window (DTWs).

Figure 11. The photopeak angular response along the detector scan plane at energies of 0.511 and 1.836 MeV for a typical detector.

Figure 12. The photopeak angular response along the detector transverse-scan plane at energies of 0.511 and 1.836 MeV for a typical detector.

Figure 13. FWHM photopeak resolution for a typical shield sector element. The large uncertainties at low energies are caused by the difficulty in determining peak widths using the broad energy channels (40 keV) for the shield element pulse-height analyzers.

Figure 14. The neutron angular response. The average energy loss per interaction is displayed at various incident angles for neutron beam energies of 32 MeV and 83 MeV.

Figure 15. OSSE on-orbit performance – Rates *vs* time. The top panel is magnetic cutoff rigidity *vs* time. Subsequent panels are single detector rates in the indicated energy bands. The eight gaps in each detector rate correspond to satellite traversals of the SAA when the detector high voltage is turned off.

Figure 16. Background spectra from 1992 Jan. 11, for detector #3. The upper spectrum was collected at times within 5400 seconds of the exit of an SAA passage. The lower spectrum was collected at least 5400 seconds from the exit of an SAA passage, effectively eliminating all SAA orbits.

Figure 17. The background-subtracted spectra from a two-week observation of the region of the sky containing the starburst galaxy, M82. Data from all four detectors have been combined. The error bars represent  $1\sigma$  statistical errors. a) Low range spectrum. b) Medium range spectrum.

Figure 18. Detector temperature and gain stability during a spacecraft maneuver to a cold-case environment. a) Detector temperature *vs* time. b) 1.332 MeV  $^{60}\text{Co}$  calibration line

centroid channel vs time over same interval as a).

Figure 19. Spectrum obtained from  $^{60}\text{Co}$  in-flight calibration system using  $\beta$ -coincidence detection.

Figure 20. OSSE  $3\sigma$  continuum sensitivity for an observation with  $5 \times 10^5$ -second livetime. Sensitivities are derived from statistical uncertainties and assumes all four detectors spend equal times on source and background. Livetime includes source and background observation time.

Figure 21. OSSE  $3\sigma$  sensitivity for the detection of narrow lines for an observation with  $5 \times 10^5$ -second livetime. As in Figure 20, sensitivity assumes four detectors spending equal times on source and background.

Figure 1: The Oriented Scintillation Spectrometer Experiment (OSSE)

Figure 2: OSSE Detector Configuration

Figure 3: The Gamma Ray Observatory Configuration

Figure 4: Example of an attitude determined by the location of the spacecraft's X and Z axes in the celestial sphere, which satisfy the spacecraft hardware constraints for a 2-week observing period beginning TBS. The field of view of the Fine Sun Sensor, solar array power zone, +X hemisphere solar constraint, and Fixed Head Star Tracker Moon exclusion circles are depicted. The locus of Sun and Moon positions during this observation are plotted as arcs in the Figure.

Figure 5: The photopeak line profile.

Figure 6: The photopeak effective area.

Figure 7: The detector resolution.

Figure 8: The measured relative light output versus energy for each of the phoswich detectors.

Figure 9: Distribution of events vs. pulse shape

Figure 10: Distribution of events as a function of pulse shape and pulse amplitude

Figure 11: The scan-plane angular response.

Figure 12: The transverse-scan angular response.

Figure 13: The shield photopeak resolution.

Figure 14: The neutron angular response.

Figure 15: OSSE on-orbit performance - Rates *vs* time. The top line is magnetic cutoff rigidity *vs* time. Subsequent lines are single detector rates in the indicated energy bands.

Figure 16: Background spectra from 11 Jan 1992, detector 3. Upper spectrum was collected at times within 5400 seconds of the exit of an SAA passage. The lower spectrum was collected at least 5400 seconds from the exit of an SAA passage, effectively eliminating all SAA orbits.

Figure 17: Two-week background-subtracted spectra.

Figure 18: Detector temperature and gain stability during a spacecraft maneuver to a cold-case environment. a) Detector temperature *vs* time. b) 1.332 MeV  $^{60}\text{Co}$  calibration line centroid channel *vs* time over same interval as a).

Figure 19: Example Co60 in-flight calibration system

Figure 20: OSSE Continuum sensitivity for four detectors spending equal times on source and background. Livetime includes source and background observation time.

Figure 21: OSSE line sensitivity for four detectors spending equal times on source and background. Livetime includes source and background observation time.

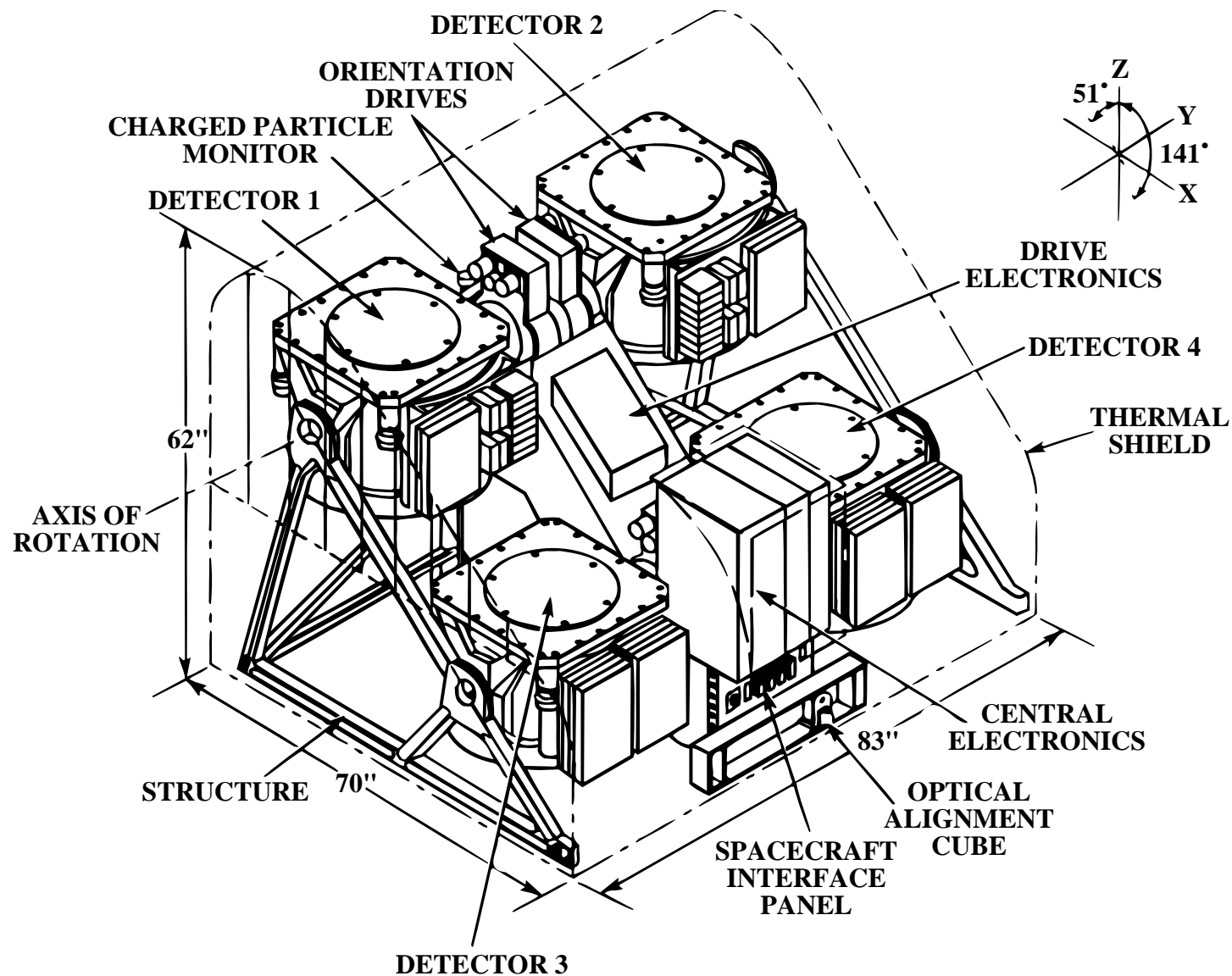


Figure 1



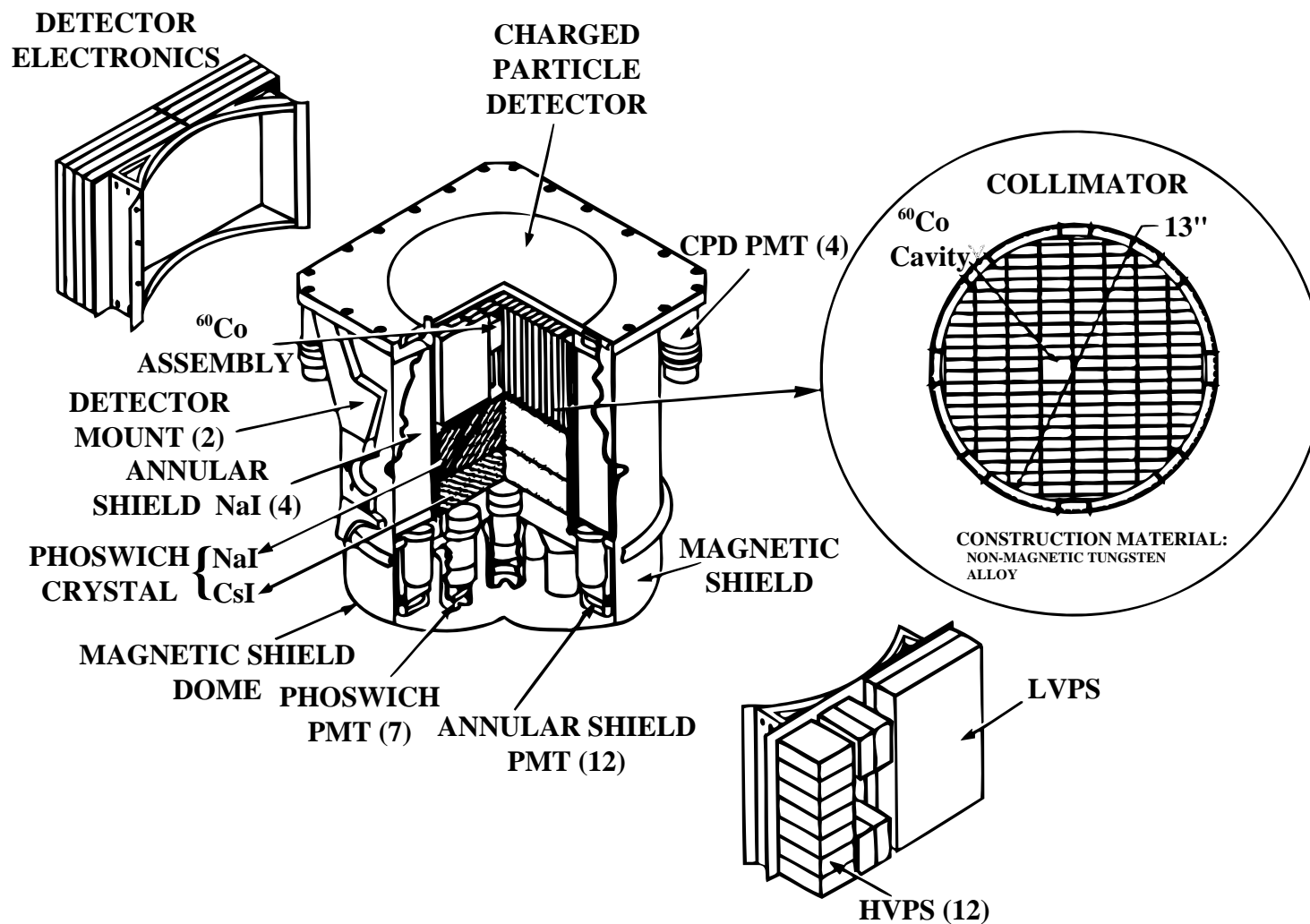


Figure 2

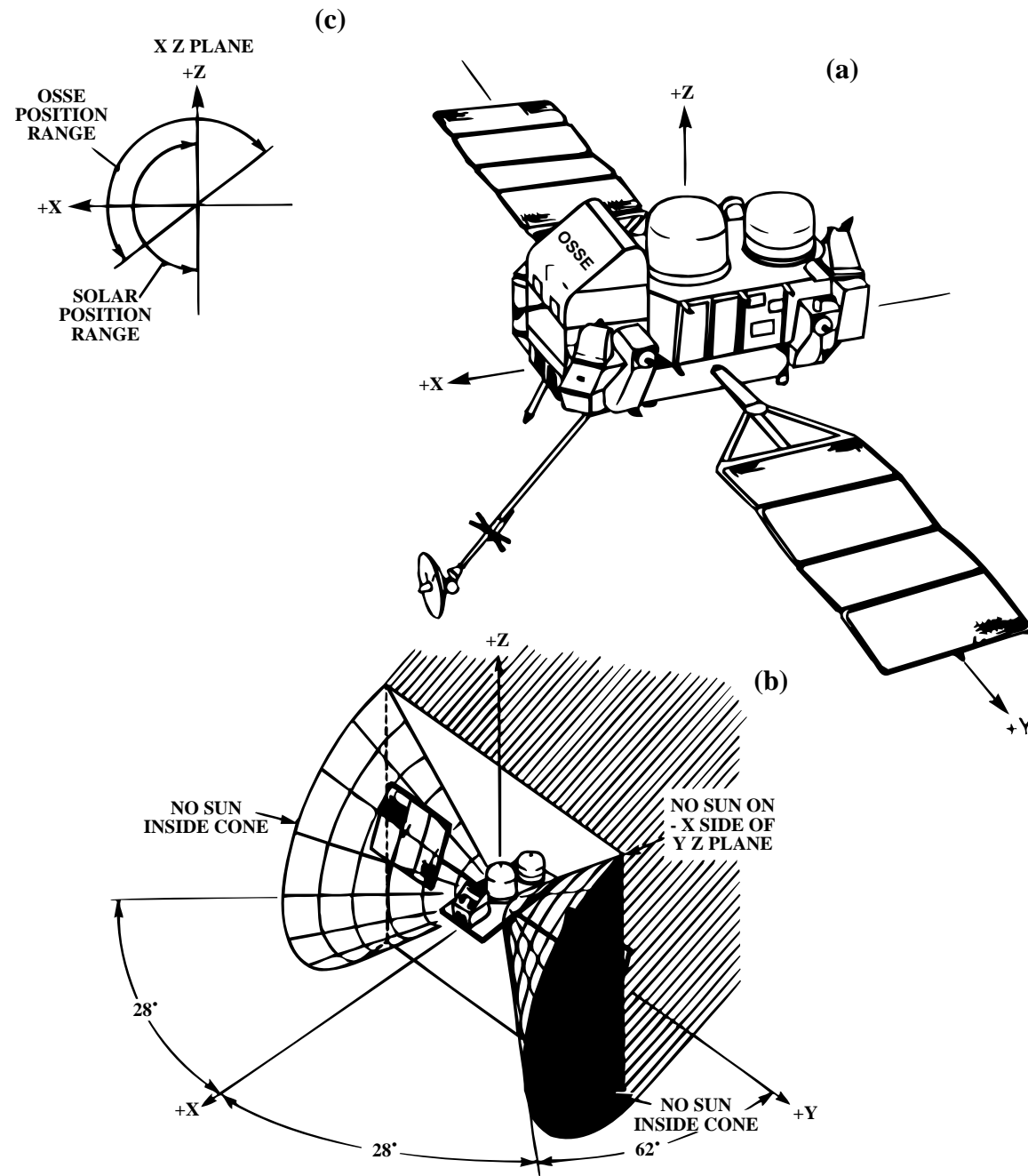
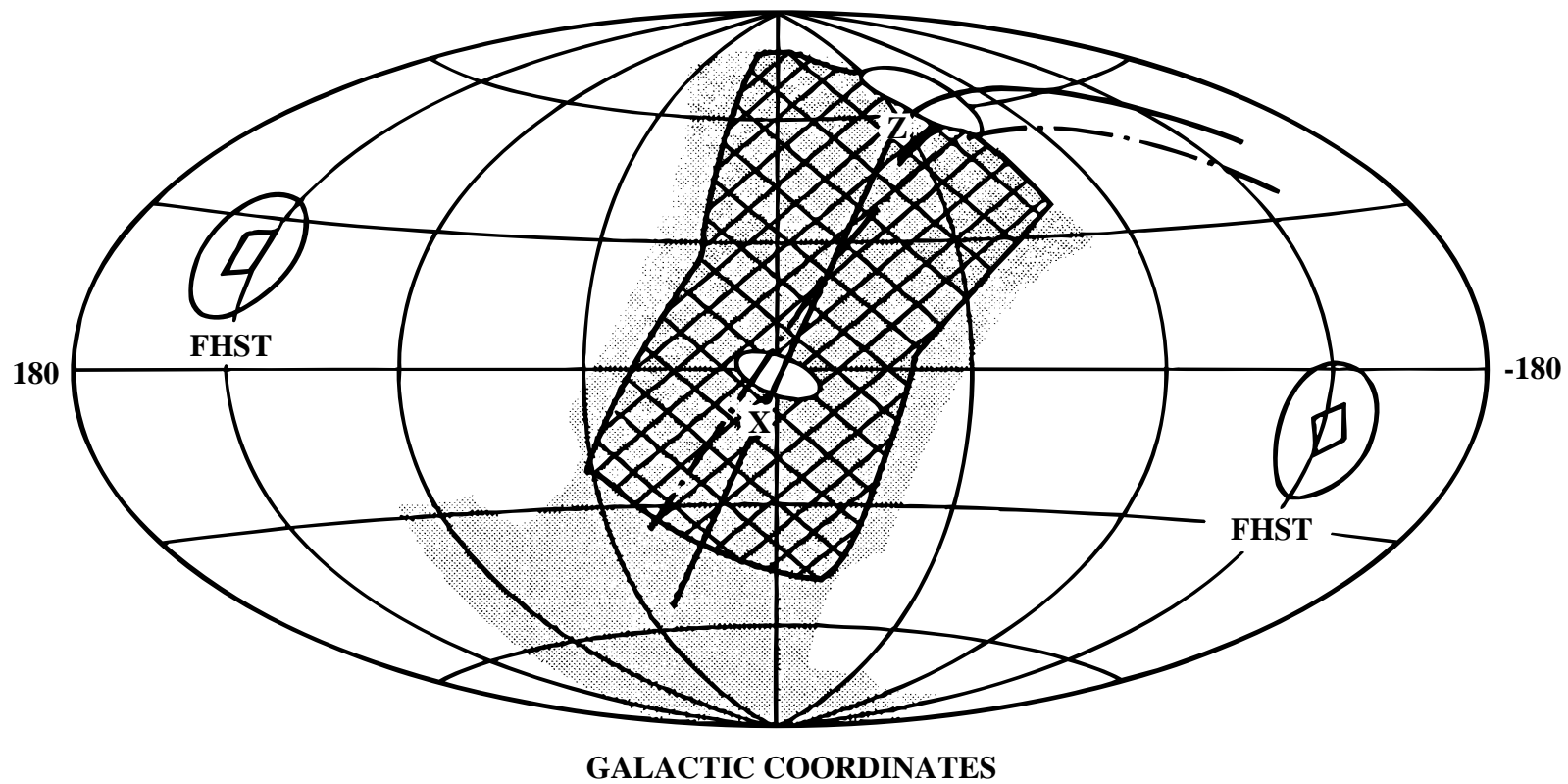





Figure 3



	<b>FOV</b>
	<b>FSS</b>
	<b>SUN CONSTRAINT</b>

	<b>SCAN RANGE</b>
	<b>MOON</b>
	<b>SUN</b>

Figure 4

